We are IntechOpen, the world's leading publisher of Open Access books
Built by scientists, for scientists

6,900
Open access books available

186,000
International authors and editors

200M
Downloads

154
Countries delivered to

Our authors are among the

TOP 1%
most cited scientists

12.2%
Contributors from top 500 universities

CLARIVATE ANALYTICS
BOOK CITATION INDEX
INDEXED

WEB OF SCIENCE™

Selection of our books indexed in the Book Citation Index
in Web of Science™ Core Collection (BKCI)

Interested in publishing with us?
Contact book.department@intechopen.com

Numbers displayed above are based on latest data collected.
For more information visit www.intechopen.com

Hard Nanocomposite Coatings, Their Structure and Properties

A. D. Pogrebnjak and V. M. Beresnev

Additional information is available at the end of the chapter

http://dx.doi.org/10.5772/50567

1. Introduction

The development of the new nanostructured coating with high hardness (40 GPa) and thermal stability (> 1200°C) is one of the most important problem of the modern material science. According to the previous experimental results it can be considered that not only grains size has strong influence on properties of the solid but also structural states of interfaces (grains boundary) [1-7]. As the quantity of atoms at grains boundary reaches about 30-50%, properties of the material are strongly depend on condition of the grains boundary: gap of the border band (in this band lattice parameter deviate from standard value), disorientation of the grains and interfaces, concentration of the defects at boundary and value of the free volume.

So, nanocrystalline materials, that contain nanosized crystallite along with rather extensive and partially disordered boundaries structure, present new properties by comparison with the large-grained materials [8-15].

These stable nanocrystalline materials can be created on base of multi-component compound, since such materials have the heterogeneous structure that include practically non-interacting phases with average linear dimension about 7-35 nm. In this case nanocrystalline materials demonstrate high thermal stability and long-term stable properties Recently, there are many papers related to the research of the structure and properties of the multi-component hard nanostructures (nanocomposite coating based on Zr-Ti-Si-N, Zr-Ti-N and Mo-Si-N etc.) were already published However, the development of the new type of the coating is

still continuing. It is well known that superhard coating can be formed on base of nc - TiN or nc-(Zr, TiN) covered with a-Si_3N_4, or BN amorphous or quasiamorphous phase, Hardness of such coating can reach 80 GPa and higher. In addition, the deposition of the coating at temperature about 550 - 600°C allows to finalize spinodal segregation along grain boundaries and hence improve properties of the coatings New superhard coatings based on Ti-Hf-Si-N featuring high physical and mechanical properties were fabricated. We employed a vacuum-arc source with HF stimulation and a cathode sintered from Ti-Hf-Si. Nitrides were fabricated using atomic nitrogen (N) or a mixture of Ar/N, which were leaked-in a chamber at various pressures and applied to a substrate potentials. RBS, SIMS, GT-MS, SEM with EDXS, XRD, and nanoindentation were employed as analyzing methods of chemical and phase composition of thin films. We also tested tribological and corrosion properties. The resulting coating was a two-phase, nanostructured nc-(Ti, Hf)N and a-Si_3N_4. Sizes of substitution solid solution nanograms changed from 3.8 to 6.5 nm, and an interface thickness surrounding a-$Si3N_4$ varied from 1.2 to 1.8 nm. Coatings hardness, which was measured by nanoindentation was from 42.7 GPa to 48.6 GPa, and an elastic modulus was E = (450 to 515) GPa. [14-18].

The films stoichiometry was defined for various deposition conditions. It was found that in samples with superhard coatings of 42.7 to 48.6GPa hardness and lower roughness in comparison with other series of samples, friction coefficient was equal to 0.2, and its value did not change over all depth (thickness) of coatings. A film adhesion to a substrate was essentially high and reached 25MPa.

Zr-Ti -Si-N coating had high thermal stability of phase composition and remained structure state under thermal annealing temperatures reached 1180°C in vacuum and 830°C in air. Effect of isochronous annealing on phase composition, structure, and stress state of Zr-Ti-Si-N-ion-plasma deposited coatings (nanocomposite coatings) was reported. Below 1000°C annealing temperature in vacuum, changing of phase composition is determined by appearing of siliconitride crystallites (β-S_3N_4) with hexagonal crystalline lattice and by formation of ZrO_2 oxide crystallites. Formation of the latter did not result in decay of solid solution (Zr,Ti)N but increased in it a specific content of Ti-component.

Vacuum annealing increased sizes of solid solution nanocrystallites from (12 to 15) in as-deposited coatings to 25nm after annealing temperature reached 1180°C. One could also find macro- and microrelaxations, which were accompanied by formation of deformation defects, which values reached 15.5 vol.%.

Under 530°C annealing in vacuum or in air, nanocomposite coating hardness increased, demonstrating, however, high spread in values from 29 to 54GPa (first series of samples). When Ti and Si concentration increased (second series) and three phases nc-ZrN, (Zr, Ti)N-nc, and α-Si_3N_4 were formed, average hardness increased to 40,8 ± 4GPa (second series of samples). Annealing to 500°C increased hardness and demonstrated lower spread in values H = 48 ± 6GPa and E = (456 ± 78)GPa.
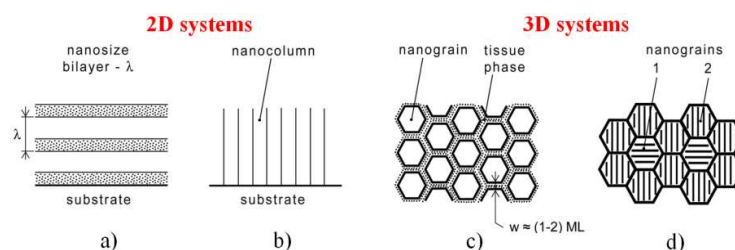
2. Enhanced hardness of nanocomposite coatings

The enhanced hardness of the nanocomposite coating Hn can be more than two times greater than that of its harder component. Main mechanisms, which are responsible for the hardness enhancement, are: (1) the dislocation-induced plastic deformation, (2) the nanostructure of materials, and (3) cohesive forces between atoms. The dislocation-induced plastic deformation dominates in the materials composed of large grains with size d < 10 nm. On the contrary, the nanostructure is dominant in materials composed of small grains with size $d \leq$ 10 nm. It means that the hardness enhancement of coating strongly depends on the grain size d, see Figure 1. From this figure it is seen that there is a critical value of the grain size $d_c \approx 10$ nm at which a maximum value of hardness Hmax of the coating is achieved. The regions of d around H_{max}, achieved at $d = d_c$, corresponds to a continuous transition from the activity of the intragranular processes at $d > d_c$, dominated by the dislocations and described by the Hall-Petch law ($H \sim d^{-1/2}$), to the activity of the intergranular processes at $d < d_c$ dominated by the interactions between atoms of neighbouring grains and/or by the small-scale sliding in grain boundaries.
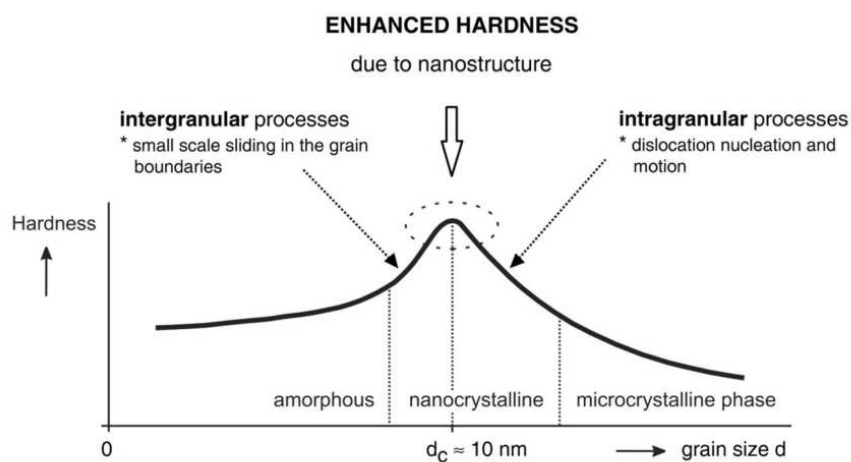
Figure 1. Schematic illustration of coating hardness as a function of the size d of grains. Adapted after reference.

In materials with the grain size $d \leq d_c$ (1) dislocations are not generated (grain size d is smaller than the length of dislocation) and (2) processes in grain boundary regions play a dominant role over those inside grains. Therefore, besides chemical and electronic bonding between atoms the nanostructure of material plays a dominant role when $d \leq d_c$. It was found that there are at least four types of nanostructures that result in the enhanced hardness of nanocomposite coatings: (1) bilayers with nanosize period λ, (2) the columnar nanostructure, (3) nanograins surrounded by very thin (~1 to 2 ML) tissue phase and (4) the mixture of nanograins with different crystallographic orientations and/or different phases, see Figure2; here $\lambda = h_1 + h_2$, h_1 and h_2 is the thickness of first and second layer of the bilayer, respectively, and ML denotes the monolayer. [1,2]

Figure 2. Schematic illustration of four nanostructures of the nanocomposite coating with enhanced hardness: (a) nanosize bilayers, (b) columnar nanostructure, (c) nanograins surrounded by a tissue phase and (d) mixture of nano-grains with different crystallographic orientation.

Individual nanostructures are formed under different conditions using eiher a sequential deposition of individual layers in the nanosize bilayers or in transition regions where the coating structure changes from crystalline through nanocrystalline to amorphous. There are three transition regions: (1) the transition from the crystalline to the X-ray amorphous material, (2) the transition between two crystalline phases of different materials and (3) the transition between two crystallographic orientations of grains of the same material. More details are given in the references.

3. Phase composition and thermal properties (stability)

3.1. Thermal stability of the properties

However, the nano- structure constitutes a metastable phase: if the temperature at which a film forms exceeds a certain threshold value T_c its material undergoes crystallization, leading to the destruction of the nanostructure and the appearance of new crystalline phases that account for the loss of unique properties by nanocomposite films for $T > T_c$. In other words, temperature T_c at which the nanostructure turns to the crystalline phase determines the thermal stability of a given nanocompo- site. However, these materials not infrequently have to be employed at temperatures above 1000°C, hence the necessity to develop new ones with maximum thermal stability in excess of 1000°C. [3-5]

3.2. Resistance to high-temperature oxidation

Oxidation resistance is a most attractive property of hard nanocomposite coatings. Oxidation resistance of hard films stronglydepends on their elemental composition. Figure 3 illustrates the increase in the film weight D_m as a function of annealing temperature T. The temperature at which D_m sharply increases is described as maximum temperature T_{max} at which film oxidation can be avoided. The higher T_{max}, the greater the oxidation resistance. All the films represented in Figure3 and characterized by a sharp growth in D_m with increasing temperature are crystalline or nanocrystalline. All of them possess oxidation resistance T_{max} below 1000°C. This is not surprising, since they are composed of grains that are constantly in contact with the air through grain boundaries at the film/substrate interface. This phenomen-

on sharply decreases oxidation resistance in the bulk of the film and is thereby responsible for the impaired efficiency of the barrier formed by the upper layer of an oxide film. For all that, an improvement is feasible by the utilization of the intergranular vitreous phase.

Thus far, only one efficacious method for increasing oxidation resistance in hard coatings is known, namely, interruption of the continuous path along grain boundaries from the coating surface to the underlying substrate across the bulk. It is possible to realize in solid amorphous films such as those formed by a new family of composites a-Si_3N_4 =MeNx with a high content (> 50 vol.%) of the amorphous phase a-Si_3N_4. This possibility is illustrated by Figure 3b, c showing a polished section of nanocomposite Ta-Si-N and Mo-Si-N films. Change in mass D_m remains practically unaltered after annealing the Ta-Si-N film at temperatures up to 1300°C (Figure 3a).
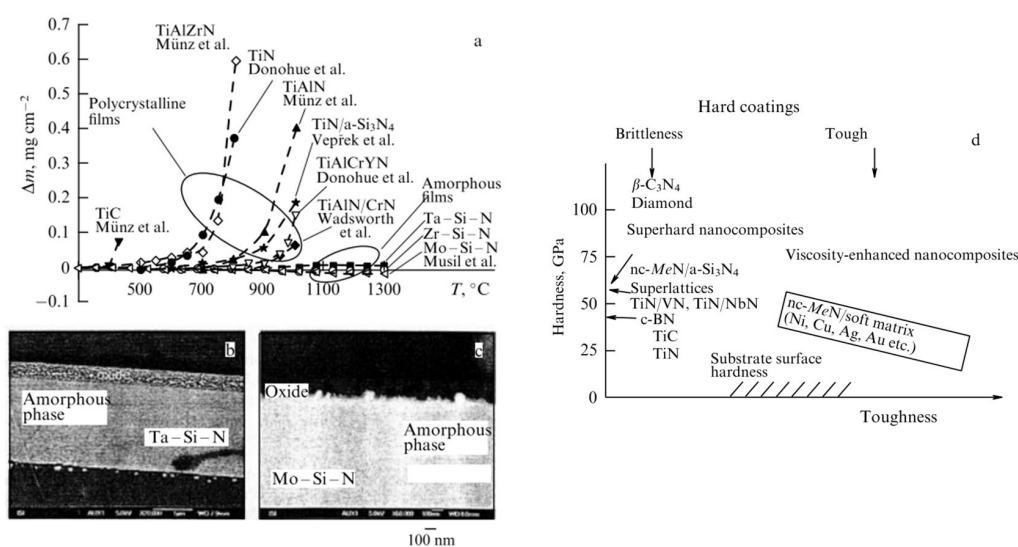
Figure 3. a) Oxidation resistance of selected hard coatings, characterized by the dependence of D_m on annealing temperature T. Polished section of Ta-Si-N (b) and Mo-Si-N (c) films on an Si (100) substrate after high-temperature annealing in flowing air atT=1300°C. (d) Classification of nanocomposites by hardness and viscosity.

3.3. Amorphous nanocomposites resistant to high-temperature oxidation

Nanocomposites containing >50 vol. % of silicon nitride are amorphous (Figure 3b, c). It can be seen that the bulk of the Ta-Si-N film possesses an amorphous structure and only the surface of the film underwent oxidation; the oxide surface layer of Ta_2O_5 is about 400 nm thick. This film exhibits the highest oxidation resistance (Figure 3a); its hardness H varies from 20 to 40 GPa. Such characteristics of Ta-Si-N films account for the wide range of their applications, e.g., as protective coatings for cutting tools.

However, a high content of silicon nitride phase alone is not sufficient to ensure resistance to high-temperature oxidation. Certain elements, like Mo, W and some others, tend to form volatile oxides released from a nanocomposite upon oxidation. This results not only in the formation of a porous structure of the oxide layer surface (Figure 3b, c) but also in impaired oxidation resistance. The pores appear because newly formed volatile oxides MoO_x diffuse

to the outside from the surface layer at T= 800– 1000°C. But the main cause of impaired oxidation resistance is disintegration of the metal nitride (MeN_x) phase in the nanocomposite; hence the importance of choosing films with proper elemental composition.

Oxidation resistance at maximum annealing temperatures can be achieved by ensuring high thermal stability of both phases in a given nanocomposite, i.e., of amorphous siliconnitride against crystallization and of metal nitride against degradation ($MeNx \rightarrow Me + N_2$). In this context, such nanocomposites as Zr-Si-N, Ta-Si-N, and Ti-Si-N with a high (>50 vol.%) silicon nitride phase content, as well as silicon oxide- and oxynitride-based nanocomposites, appear especially promising. [4]

4. Effect of thermal annealing in vacuum and in air on nanograin sizes in hard and superhard coatings Zr-Ti-Si-N

Analyzing phase composition of Zr-Ti-Si-N films, we found that a basic crystalline component of as-deposition on state was solid solution (Zr, Ti)N based on cubic lattice of structured NaCl.

Crystallites of solid (Zr, Ti)N solution underwent compressing elastic macro stresses occurring in a "film-substrate" system. Compressing stresses, which were present in a plane of growing film, indicated development of compressing deformation in a crystal lattice, which was identified by a shift of diffraction lines in the process of angular surveys ("$\sin2\psi$ – method") and reached – 2.93 % value. With E ≈ 400 GPa characteristic elastic modulus and 0.28 Poisson coefficient, deformation value corresponded to that occurring under action of compressing stresses $\sigma_c \approx 8.5$ GPa.

Figure 4 shows morphology of surface on base (Zr-Ti-Si)N formed with U = −150 V, P = 0,8 Pa. Investigated, that a change in direction of increasing the potential applied to the substrate, the roughness decreases. [5]
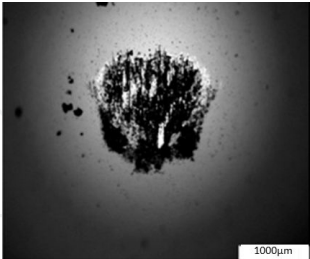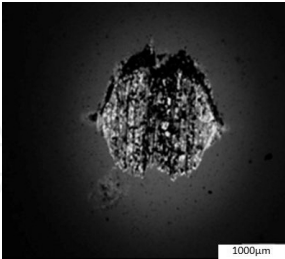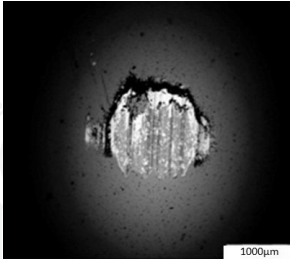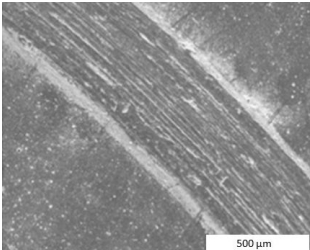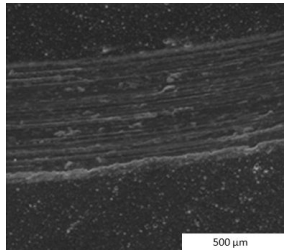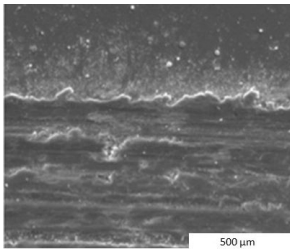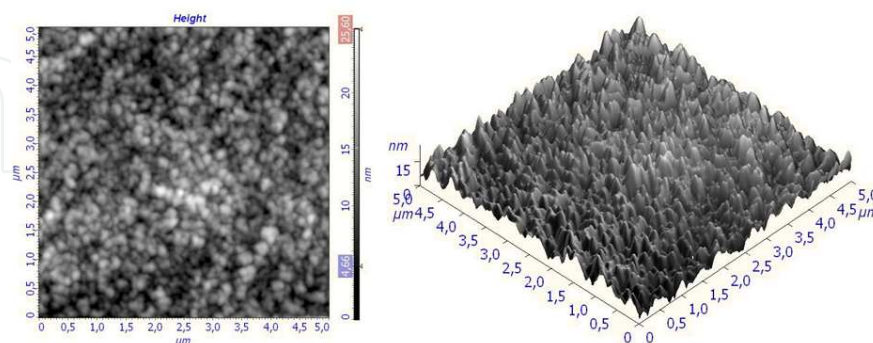

Figure 4. Surface morphology of coatings on base (Zr-Ti-Si)N with U= −150V, P=0,8 Pa.

The resulting coatings have the following hardness: TiN (H = 28 GPa and E = 312 GPa); Ti-Si-N (H = 38-39 GPa, E = 356 GPa); Ti-Zr-Si-N hardness values H = 38... 41 GPa, E = 478 GPa. Tables 1 and 2 show the results of tribological tests.

Coatings	Temperature tests, °C	Wear coating factor, mm³/nm	Wear factor of the sample, mm³/nm	f_{mp}
Ti-Zr-Si-N	30	$7,59 \times 10^{-5}$	$1,93 \times 10^{-5}$	0,80
	300	$2,22 \times 10^{-5}$	$3,14 \times 10^{-5}$	0,71
	500	$1,49 \times 10^{-5}$	$2,81 \times 10^{-5}$	0,58
Ti-Zr-Si-N (a)	30	$7,559 \times 10^{-5}$	$3,214 \times 10^{-5}$	0,805
Ti=22,73	300	$1,84 \times 10^{-5}$	$4,726 \times 10^{-5}$	0,836
Zr=2,12 Si=3,05	500	$1,47 \times 10^{-5}$	$3,047 \times 10^{-5}$	0,582
Ti-Zr-Si-N (b)	30	$6,75 \times 10^{-5}$	$3,304 \times 10^{-5}$	0,793
Ti=28,32	300	$3,62 \times 10^{-5}$	$3,83 \times 10^{-5}$	0,813
Zr=2,67 Si=3,64	500	$1,985 \times 10^{-5}$	$2,749 \times 10^{-5}$	0,585
Ti-Zr-Si-N (c)	30	$7,697 \times 10^{-5}$	$3,279 \times 10^{-5}$	0,877
Ti=27,46	300	$2,635 \times 10^{-5}$	$3,486 \times 10^{-5}$	0,825
Zr=2,51 Si=3,76	500	$1,955 \times 10^{-5}$	$2,749 \times 10^{-5}$	0,632
Ti-Si-N	30	$7,69 \times 10^{-5}$	$3,28 \times 10^{-5}$	0,88
	300	$2,63 \times 10^{-5}$	$3,49 \times 10^{-5}$	0,82
	500	$1,95 \times 10^{-5}$	$2,75 \times 10^{-5}$	0,69
TiN	30	$6,75 \times 10^{-5}$	$3,30 \times 10^{-5}$	0,81
	300	$3,62 \times 10^{-5}$	$3,51 \times 10^{-5}$	0,87
	500	$5,16 \times 10^{-5}$	$3,83 \times 10^{-5}$	0,91

Table 1. The results of tribological properties of nanocomposite coatings.

Options	T=30°C	T=300°C	T=500°C
Sample			
Friction track			

Table 2. The macrostructure of the surface of the nanocomposite coatings Ti-Zr-Si-N.

The chamber pressure is insignificant effect on the morphology, but noted that the increase in gas pressure in the chamber leads to a decrease in surface roughness. Figure 4 shows the optimal parameters of the chamber pressure and the potential applied to the substrate (U = −150 V, P = 0,8 Pa) under which the maximum peak is 16 nm.

We should also note that such high stresses characterize nitride films, which were formed under deposition with high radiation factor, which provided high adhesion to base material and development of compression stresses in the film, which was stiffly bound to the base material due to "atomic peening"- effect. [6-12]

At sliding speeds 10 cm/s is a normal abrasive oxidative wear friction. The structural-phase state coverings plays a crucial role in the processes of wear and temperature dependent. At temperatures of 30°C tests are covering adhesive interaction with the counterbody - there is a rough surface topography of the coating. At temperatures of 300°C tests for coatings based on Ti-Si-N and Zr-Ti-Si-N coating decreases the wear and wear counterface increases. With further increase in temperature to 500°C decreases the wear coating Ti-Si-N and Zr-Ti-Si-N, increases their durability. This leads to a change in the conditions of the processes occurring in the contact zone due to changes in the structure of surface layers.

Qualitative changing of phase composition was observed in films under vacuum annealing at T_{an} > 1000°C. Appearance of zirconium and titanium oxides was related to oxidation relaxation under coating surface interaction with oxygen atoms coming from residual vacuum atmosphere under annealing.

Figure 5 shows the results of RBS analysis on the samples obtained were coated with Ti-Zr-Si-N. The beam energy $^+$He ions is not sufficient for the analysis of the total film thickness, but the peaks of Ti and Zr are well separated and can be seen that the concentration of Ti and Zr is almost uniformly distributed over the depth of coating. [10-12]
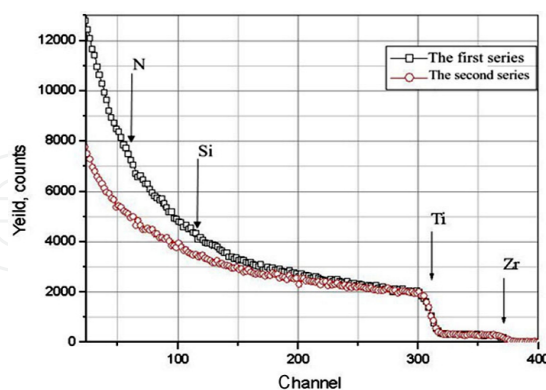

Figure 5. Energy spectra of Rutherford ion backscattering (RBS) for thin coating Zr-Ti-Si- N.

But still, Si concentration was not less than 7 at.%, while that of N might reach more than 15 at.%.

Figure 6. shows scratch properties of Zr-Ti-Si-N. The friction coefficient (μ) between two solid surfaces is defined as the ratio of the tangential force (F) required to produce sliding divided by the normal force between the surfaces (N). Normal force F_n (occasionally N) is the

component, perpendicular to the surface of contact, of the contact force exerted on an object by the surface. Acoustic Emission is a naturally occurring phenomenon whereby external stimuli, such as mechanical loading, generate sources of elastic waves. Penetration Depth is a measure of how deep light or any electromagnetic radiation can penetrate into a material. It is defined as the depth at which the intensity of the radiation inside the material falls to $1/e$ (about 37 %) of its original value at (or more properly, just beneath) the surface.
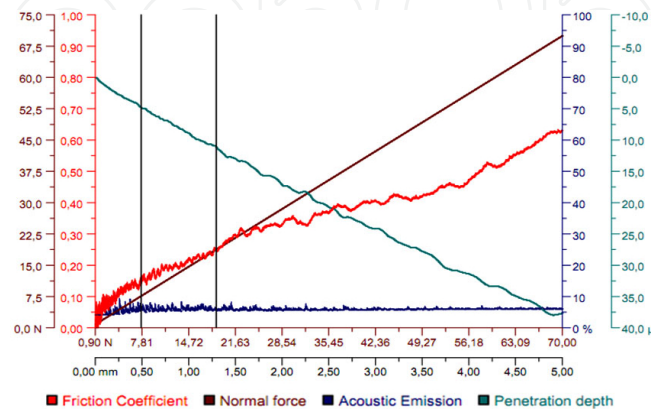
Figure 6. Scratch properties of Zr-Ti-Si-N: friction coefficient, normal force, acoustic emission, penetration depth.

Under annealing temperatures below 1000°C, coatings phase composition remained practically unchanged. One could not only changed width of diffraction lines and their shift to higher diffraction angles. The latter characterizes relaxation of compressing stresses in coatings. Changed diffraction lines were related to increased crystalline sizes (in general) and decreased micro-deformation.

Three-dimensional islands on the surface of the films with columnar structure are output on the surface of the ends of individual grains (Figure 7). It is seen that the roughness depends on the conditions of their chemical composition and the parameters of the wasp-assertion. Undulation surfaces associated with the mechanism of growth, with the formation of separate islands on the surface (Volmer-Weber mechanism)[10,11].
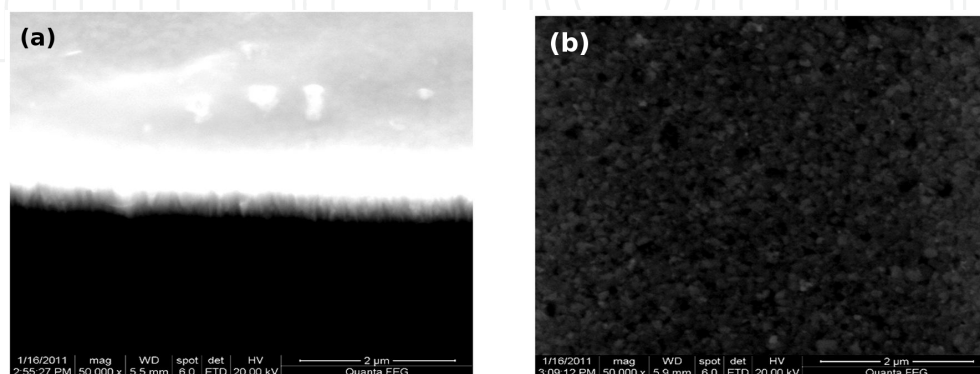
Figure 7. Coating Ti-Zr-Si-N with a columnar structure: (a) a cross-section coating, (b) surface topography of the coating.

In such a way, hardness, which was increased in the process of annealing, seems to be related to incomplete spinodal phase segregation at grain boundaries resulting from deposition of Zr-Ti-Si-N-(nanocomposite). Annealing stimulated spinodal phase segregation, forming more stable modulated film structures.

Figure 8 shows chemical composition over coating cross-section. Spectra indicate that N concentration changed from 3.16 to 4.22 wt.%, Si concentration was about 0.98 to 1.03 wt.%, Ti was 11.78 to 13.52 wt.% and that Zr = 73.90 to 77.91 wt.%. These results indicated that amount of N is essentially high, and this allowed it to participate in formation of nitrides with Zr, Ti, or (Zr, Ti)N solid solution. Si concentration was low, however, results reported by Veprek et al. indicated Si concentration as high as 6 to 7at.%, which was enough to form siliconitride phases.
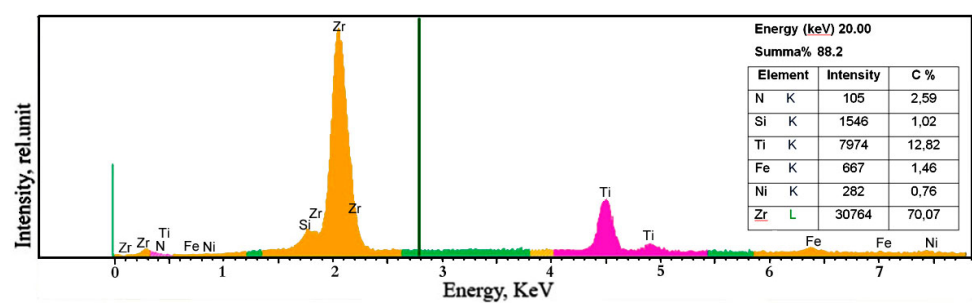
Figure 8. Data of microanalysis for point of Zr-Ti-Si-N (Ti≈12%) nanocomposite coating surface. (fifth series)

Changes occurred under macrodeformation of crystallites of basic film phase – (Zr, Ti)N solid solution. Compressing deformation of crystallite lattices increased, which seemed to be related to additional new crystalline components, which appeared in film material: oxides and siliconitrides. In the lattice itself, a period decreased corresponding to increased Ti concentration. Ordered atoms in metallic (Zr/Ti) sublattice of solid solution increased from 8.5 to 21 at.%.

In this temperature range, crystallite size increased from 15 to 25 nm, crystallite lattice microdeformation increasing non-essentially up 0.5 to 0.8 %. Table 3 summarizes substructure characteristics of (Zr, Ti)N solid solution crystallites.

Parameters of structure	After deposition	$T_{an} =$ 300ºC vacuum	$T_{an} =$ 500ºC vacuum	$T_{an} =$ 800ºC vacuum	$T_{an} =$ 1100ºC vacuum	$T_{an} =$ 300ºC air	$T_{an} =$ 500ºC air
a_0, nm	0,45520	0,45226	0,45149	0,45120	0,45064	0,45315	0,45195
□, %	-2,93	-2,40	-1,82	-1,01	-1,09	-2,15	-1,55
<□"/, %	1,4	1,0	0,85	0,5	0,8	0,95	0,88
□ def. pack.	0,057	0,085	0,107	0,155	0,150	0,090	0,128

Table 3. Changes of structure and substructure parameters occurring in ion-plasma deposited coatings of Zr-Ti-Si-N system in the course of high-temperature annealing in vacuum and in air.

In comparison with vacuum annealing, air one is characterized by a decreased of phase stability above 500°C – 600°C. Above these temperatures, one observed formation of oxides resulting in film destruction and total film destruction at 830°C.

Processes occurring in the film under annealing temperature below 600°C were similar to those occurring under vacuum annealing under the same temperature interval: they were characterized by decreased lattice period, lower values of micro- and macrodeformations accompanied by increasing concentration of deformation packing defects in metallic sublattice of solid solution.

Qualitative changing of phase composition was observed in films under vacuum annealing at T_{an} > 1000°C. Figure 9 shows characteristic diffraction curve, which was taken under 30min annealing at T_{an} = 1100°C. Under high-temperature annealing, in addition to (Zr, Ti)N nitrides (which period was close to ZrN lattice) and (Ti, Z)N (which period was close to TiN lattice), we observed diffraction peaks from zirconium oxide crystallites (ZrO$_2$, according to JCPDS Powder Diffraction Cards, international Center for Diffraction Data 42-1164, hexagonal lattice) and titanium oxide (TiO, JCPDS 43-1296, cubic lattice), and, probably, initial amorphous β-Si$_3$N$_4$ phase crystallites (JCPDS 33-1160, hexagonal lattice). Appearance of zirconium and titanium oxides was related to oxidation relaxation under coating surface interaction with oxygen atoms coming from residual vacuum atmosphere under annealing.
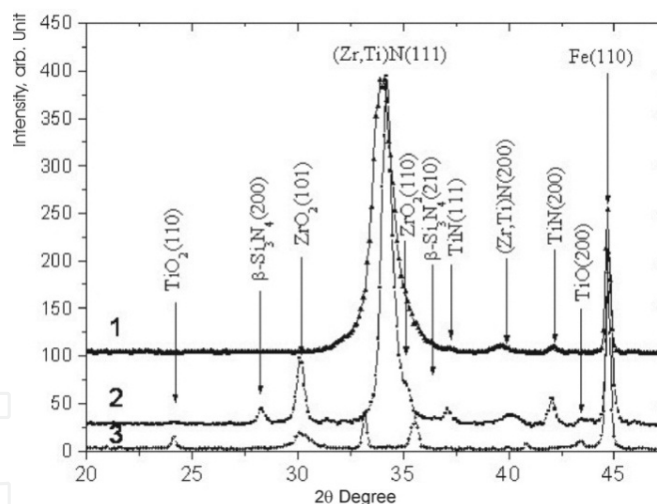
Figure 9. Region of X-ray diffraction spectra taken for the condensates of Zr-Ti-Si-N system after deposition (1); after 30 min annealing in vacuum, under T_{an} = 1180°C (2), and under T_{an} = 800°C in air (3). Three peaks, which are not designated in the curve, are for an oxide of Fe$_2$O$_3$ substrate (JCPDS 33-0664).

In solid solution, hardness increased due to increasing Ti concentration and appearance of Si$_3$N$_4$ phase. In initial state, after deposition, those samples, which phase composition included three phases (Zr,Ti)N-nc, ZrN-nc, and α-Si$_3$N$_4$), hardness was H = 40,6 ± 4 GPa; E = 392 ± 26 GPa. 500°C annealing increased H and E and decreased spread in hardness values, for example, H = 48 ± 6 GPa and E = (456 ± 78GPa), see Table 4.

Parameters	After deposition	T_{an} =300ºC vacuum	T_{an} =500ºC vacuum
H, Gpa	40,8±2	43,7±4	48,6±6
E, Gpa	392±26	424±56	456±78

Table 4. Changes of hardness and elastic modulus in nanocomposite coating before and after annealing.

Method X-ray scanning, demonstrated shift and broadening of diffraction peaks. Highest content of packing defects indicated shift of most closely packed planes in a fcc-sublattice (111) with respect to each other and became pronounced under vacuum annealing at T_{an} = 800 to 1100°C reaching 15.5 vol.%. As it is seen from "loading-unloading" curves and calculation results, under annealing in vacuum at 500°C, nanohardness of Zr-Ti-Si-N films was H = 46 GPa (dark circles).

When Ti and Si concentration increased and three phases nc-Zr-N, (Zr, Ti)N-nc, and α-Si$_3$N$_4$ were formed, average hardness increased to 40,8 ± 4 GPa. Figure 10 shows that in initial state, Zr-Ti-Si-N film (as received) had 40.8 GPa nanohardness. After annealing (a dark dotted curve) at 500°C in vacuum, coating nanohardness reached H = 55.3 GPa. [9,11,13]
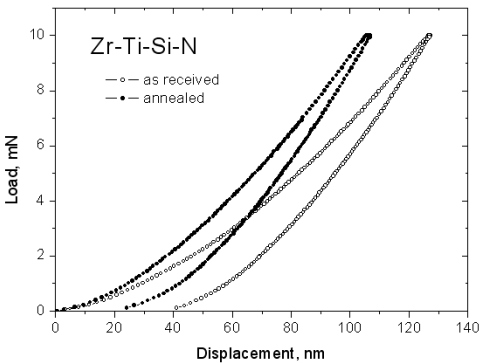
Figure 10. Load-displacement curves for as received and annealed (500°C) Zr-Ti-Si-N Effect of 500°C annealing in vacuum on nanohardness.

5. General regularities and difference of nanocomposite coatings based of Zr, Ti, Hf, V, Nb metals and their combinations

Ti-Hf-Si-N films were deposited on steel 3 substrate (20 mm diameter and 3 mm thickness) with the help of vacuum source in the HF discharge of the cathode, sintered from the Ti-Hf-Si. In order to obtain nitride, atomic N was flooded to the chamber at different pressure and substrate potential. Deposition conditions are presented in Table 5. Bulat 3T-device with generator was used for the deposition of samples. A bias potential was applied to the substrate from a HF generator, which generated impulses of convergent oscillations with ≤ 1 MHz frequency, every duration of the impulse was 60μs, their repetition frequency about 10 kHz. Due to HF diode effect the value of negative auto bias potential at substrate was about 2÷3 kV.

N°	Lattice parameter, nm	Average size of crystallite, nm	Hf content in solid solution (HfTi) coming from the size of period ***, at.%	Hardness, GPa	Nitrogen pressure in chamber, Pa	Substrate potential, V
23(100V,separated)	0.4294*	6.7**	19	42.7	0,7	-200
28(200B, non separated)	0.4430	4.0	65	37,4	0,6-0,7	-200
35 (100V, non separated)	0.4437	4.3	69	38,3	0,6÷0,7	-100
37 (200V, separated)	0.4337	5.0	33	48.6	0,6	-100
31 (200V, separated)	0.4370	3.9	45	39,7	0,3	-200

*- in textured crystallites of samples (series№23) with texture axis (220), the period is more than 0.43602 nm, which can be connected with high Hf content in them (about 40 at%).

**- in the texture axis direction of textured crystallites the average size is larger (10.6 nm).

***- Calculation was carried out according to Vegard rule from period values of solid solution (the influence of macrostresses on the change of diffraction lines was not taken into account).

Table 5. Results of study of: the Ti-Hf-Si-N film depositing parameters; the lattice constant; the crystallite size; the hardness of different series of samples.

Secondary mass-spectrometers SAJW-0.5 SIMS with quadruple mass analyzer QMA-410 Balzers and SAWJ-01 GP-MS with glow discharge and quadruple mass analyzer SRS-300 (Poland, Warszawa) was used for studying of the samples chemical composition. In order to obtain complete information about samples chemical composition, 1.3 MeV ion RBS spectrometers equipped with 16 keV resolution detectors was applied. Helium ion dose was about 5 μC. Standard computer software was used for the processing of the RBS spectra, as a result the depth distribution of the concentration of compound components was plotted.

The research of the mechanical properties of the samples was carried out by the nanoindentation methods with the help of Nanoindenter G200 (MES Systems, USA) equipped with Berkovich pyramid (radius about 20 nm). An accuracy of measured indentation depth was ±0.04 nm. Measurements of the nanohardness of the samples with coating were carried out till 200 nm depth, in order to decrease influence of the substrate on the nanohardness value. The depth of indentation was substantially less than 0.1 of coating depth. XRD analysis was performed using DRON-4 and X´PertPANalitical (Holland) difractometers (step size 0.05°, speed 0.05°C, U = 40 kV, I=40 mA, emitter-copper)[11].

The cross-sections of the substrates with coatings were prepared by the ion beam. Further analysis of surface morphology, structure and chemical composition of these cross sections was carried out by the scanning ion-electron microscope Quanta 200 3D.

For determination of adhesion/cohesion strength, firmness to the scratching, and also for research of destruction mechanism, the scratch-tester REVETEST was used (CSM Instruments).

Prior to analysis of XRD data, it should be noted that for better understanding of processes occurred at near-surface region during deposition it is necessary to compare formation heats of the probable nitrides. According to standard heats of formation of such nitrides are next: $\Delta H_{298}(HfN) = -369.3$ kJ/mole, $\Delta H_{298}(TiN) = -336.6$ kJ/mole, $\Delta H_{298}(Si_3N_4) = -738.1$ kJ/mole, i.e. values of the formation heats are quite large and negative. It indicates high probability of those systems formation during all stages of transport of the material from target to substrate. In addition, proximity of formation heats for TiN and HfN establish conditions for formation of the sufficiently homogenous (Ti,Hf)N solid solution.

The XRD-analysis revealed the presence of two-phase system. This system was determined as the substitutional solid solution (Ti,Hf)N because diffractions peaks of this phase are located between peaks related to mononitrides TiN (JCPDS 38-1420) and HfN (JCPDS 33-0592). The diffused peaks with less intensity at 2θ values from 40° to 60° are related to the α-Si_3N_4 phase (Figure 11).

According to Figure 11, in direct-flow mode without separation the non-textured polycrystalline coatings are formed. Rather high intensity of the peaks at XRD-patterns of (Ti,Hf)N solid solutions is attributed to relatively large concentration of hafnium, which has larger reflectance value than titanium.
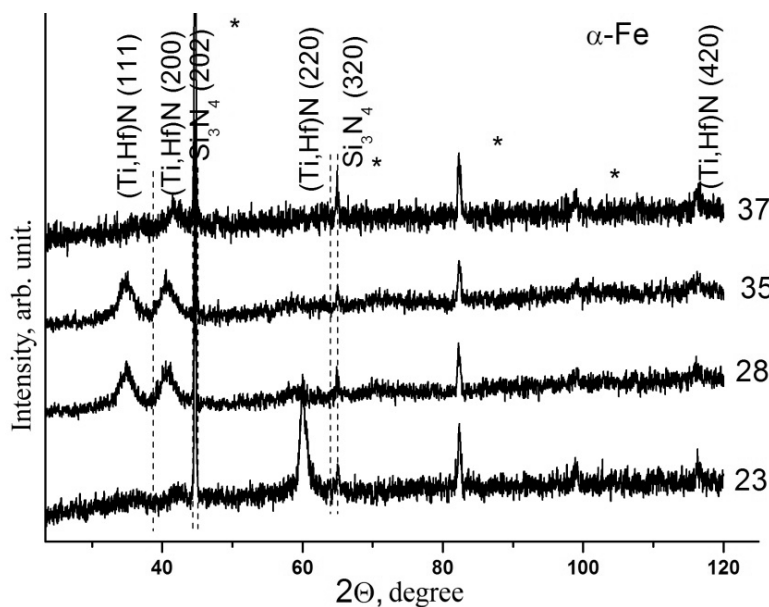
Figure 11. XRD spectra of the coatings deposited on a steel substrate at modes (1-(23) – 100V, separated, 2-(28)-200V, non-separated, 3 (35)-100V, non-separated, 4 (37)-200V, separated).

In case of beam separation the coatings have different texturation. At low substrate potential (100 V) coatings have [110] texture, and coatings consist of textured and non-textured crystallites. The volume content of textured crystallites is about 40% of total amount of the crystallites, and their lattice parameter enlarged in comparison to non-textured crystallites. We suppose that the increased lattice parameter may be caused by the inhomogeneous distribution (mainly in the lattice sites of the textured crystallites) of the hafnium atoms in coating.

At the same time, coating texture leads to increasing of the average grains size of the crystallites along the direction of particle incidence (perpendicular to the growth front). For example, in non-textured fraction of the crystallites the average grains size is about 6.7 nm, whereas in textured crystallites the value of the average grains size is substantially more, namely 10.6 nm. It should be noted that such coatings have the highest nanohardness.

The increase of the substrate potential up to 200 V caused the decrease of average grains size to 5.0 nm. The volume content of textured crystallites is also significantly decreased (less than 20%), moreover the texture axis changed from [100] to [001]. However in this case the lattice parameter is 0.4337 nm and it is larger than for the nontextured fraction in samples obtained at low substrate potential.

According to Vegard law this value of the lattice parameter corresponds to 33 at.% of Hf in metallic (Hf,Ti) solid solutions of the nitride phase (the reference data of the lattice parameters of aTiN=0.424173 nm (JCPDS 38-1420) and aHfN = 0. 452534 nm (JCPDS 33-0592) was used).

However, as a rule, the compressive stresses in coatings caused the decrease of the angles of corresponding diffraction peaks during θ-2θscan, hence calculated values of lattice parameter can be overestimated. As a result inaccuracy of the calculation of Hf concentration in solid solutions can achieve about 5-10 at. %. Therefore presented results can be considered as estimation of upper limit of the Hf concentration in solid solution.

All above mentioned results are related to samples obtained at typical pressure (0.6-0.7) Pa, whereas in a case of coating deposition at 200 V substrate potential in mode of separation (set of samples 31), the decreasing of pressure up to 0.3 Pa caused the increase of relative content of heavy Hf atoms in coatings. In addition, the average grains size of the crystallites decreased with pressure.

Indeed, the decrease in pressure should be accompanied by decrease of the probability of energy loss of atoms during collision between targets and substrate. Thus, atoms at substrates have relatively high energy which can promote secondary sputtering and radiation defect formation. So, secondary sputtering leads to decrease of relative content of heavy Hf atoms, while radiation defect formation provide the decrease of grain size with the increase of nucleus amount.

The coatings obtained under the typical pressure (0.6-0.7) Pa in case of non-separated beam (direct-flow mode) have considerably larger lattice parameter; it can be explained by the high concentration of heavy Hf atoms. [14]
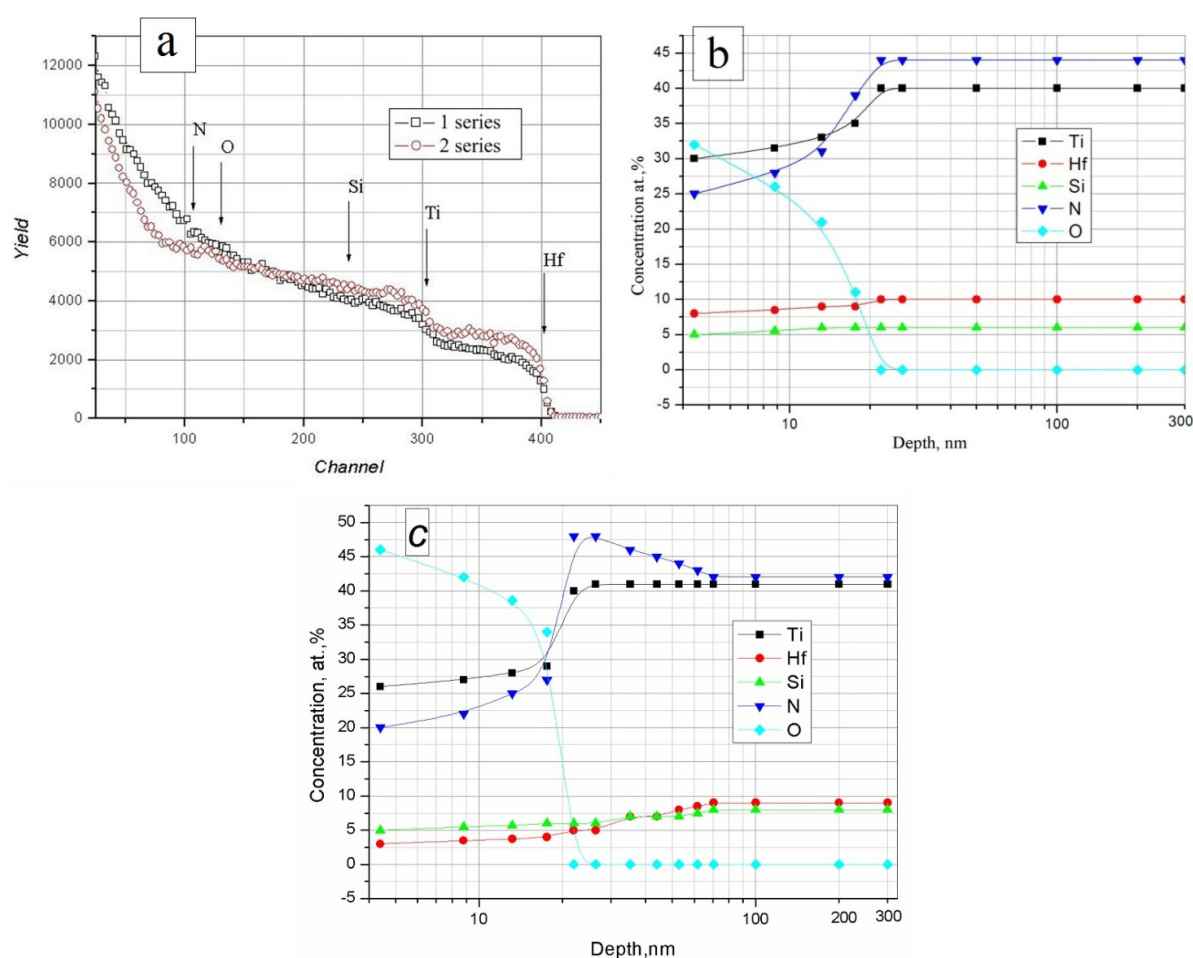
Figure 12. a) RBS spectra of He+ with 1,3 MeV energy, obtained from steel sample with Ti-Hf-Si-N film: curve 1-potential 100V, p=0,6 Pa, curve 2 - potential 200V, p=0,7 Pa. (b) The depth profiles of elements in the Ti-Hf-Si-N coating, obtained from RBS spectrums (Figure12a). Considering that atomic density of layer is close to atomic density of titanium nitride. (c) The depth profiles in the Ti-Hf-Si-N coating obtained from spectrums (2) on Figure12a (mode 2).

Apparently, the more intensive direct-flow mode leads to the increase of the nucleus density and hence to the decrease of average grain size. In addition, more pronounced decrease of the grains size is caused by the higher substrate potential -200 V. It is obviously because increasing of radiation factor leads to the dispersion of structure. The results of the research of chemical composition of the Ti-Hf-Si-N nanostructured superhard films by the several methods are shown in Figure 12 (RBS(a), SIMS(b), GT-MS(c)). As follows from Figure 12 a, b (curves 1) chemical composition of samples from first set is $(Ti_{40}$-Hf_9-$Si_8)$ N_{46}.

It is well known that RBS method is a reference for the determination of concentration of the elements with high atomic number and films thickness; also RBS is a nondestructive method. Whereas SIMS is more sensitive method (threshold of sensitivity is about 10^{-6} at.%). Therefore comparison of results obtained by the RBS, SIMS and GT-MS methods allows obtaining of more reliable data of the chemical composition and depth distribution of the concentration of compound components. This joint analysis let us to study the chemical composition along the films cross-section from the surface to the films-substrates interfaces.

Analysis of samples chemical composition also includes measurement of the concentration of uncontrolled oxygen from the residual chamber atmosphere.

As a result we have determined chemical composition $(Ti_{40}-Hf_9-Si_8)N_{46}$of the coatings with thickness about 1μm±0.012 μm. The second set of Ti-Hf-Si-N samples was obtained at increased bias potential (-200 V) under the pressure of 0.3 Pa.

Joint analysis of the films chemical composition by the RBS (Figure 12a curves 2), EDXS and SIMS methods allowed determining of stoichiometry of films as $(Ti_{28}-Hf_{18}-Si_9) N_{45}$.

The measuring of nanohardness by the triangular Berkovich pyramid (Figure 13) showed that the nanohardness of the samples from the first set is H=42.7 GPa and elastic modulus is E=390±17 GPa (Figure 13), and for the Ti-Hf-Si-N samples from the second set, the nanohardness is H=48.4±1.4 GPa and elastic modulus is E=520±12 GPa.

The XRD-analysis of the phase composition and calculation of the lattice parameter allow us to consider that the two-phase system based on substitutional solution (Ti, Hf)N and α-Si_3N_4 is formed in films.

It was determined that lattice parameter of the solid solution increased with pressure and does not depend on substrate potential. The minimal lattice parameter of the (Ti, Hf)N solid solution was observed in samples from the 23 set.
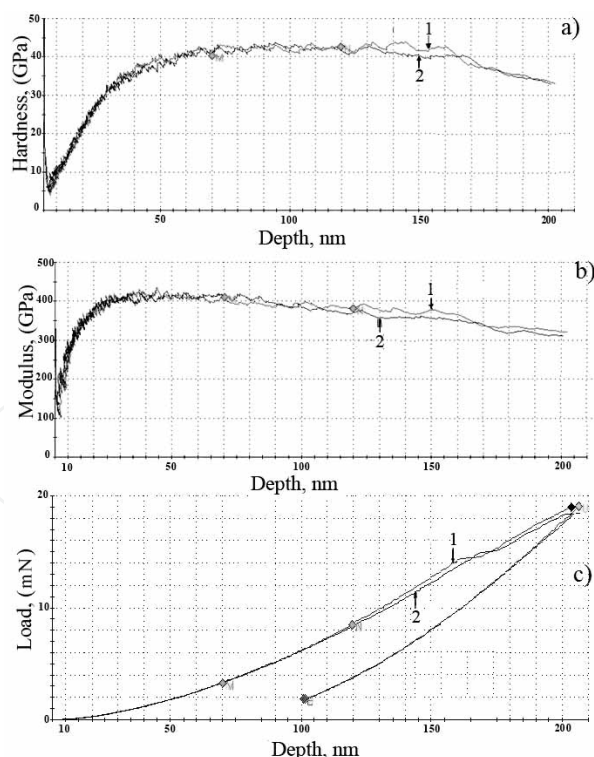
Figure 13. The dependence of hardness H(GPa) (a) on the depth of indentation, (b) the dependence of elastic modulus E(GPa) on the depth of indentation (the regions of H, E measurements are marked with points, series of probes are marked by numbers).

The calculation by the Debye-Scherer method showed that the size of nanograins of the $(Ti_{28}-Hf_{18}-Si_9)$ N_{45} samples from the second set is 4 nm, and it is approximately 1.5 times less than for the first set of the samples. Moreover size (thickness) of amorphous (or quasiamorphous) interlayer was also less than for the first set of the samples (Table 6).

The preliminary results of the HRTEM analysis of samples with nanostructured superhard films are revealed that size of nanograined phase is about 2-5 nm, this result is in correlation with XRD data. In addition it was determined that size of α-Si_3N_4 interlayer, which is envelop the (Ti, Hf)Nnanograins, is about (0.8-1.2) nm.

The properties (hardness, elastic modulus) of Ti-Hf-Si-N samples from the first set were not changed during the storage time from 6 to 12 month.

An analysis of thermal and oxidation resistance was not performed. Therefore it is difficult to conclude that the process of spinodal segregation at the grain boundaries is fully completed. In addition the substrate temperature during the deposition was not more than 350÷400°C, and it is substantially less than full segregation temperature (550÷620°C).

Detailed study of such parameters as coefficient of friction, acoustic emission and depth penetration, were carried out with all samples.

Three-dimensional islands on the surface of the films with columnar structure are output on the surface of the ends of individual grains (Figure 14). It is seen that the roughness depends on the conditions of their chemical composition. Undulation surfaces associated with the mechanism of growth, with the formation of separate islands on the surface (Volmer-Weber mechanism).
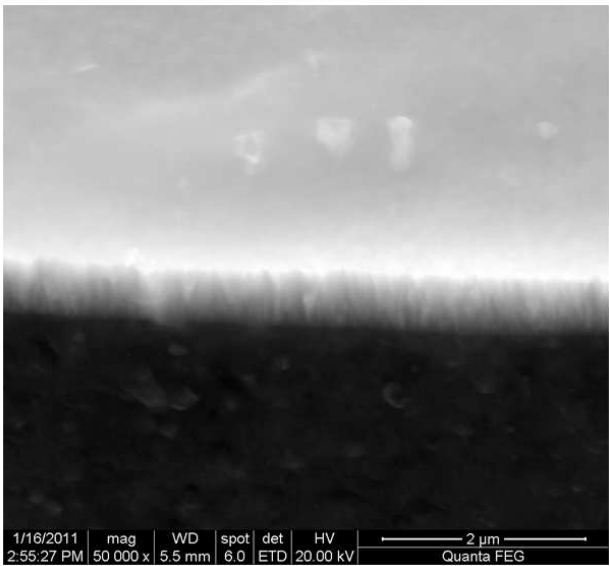
Figure 14. Cross-section of coating Ti-Hf-Si-N with a columnar structure.

The friction coefficientof the sample in the initial stage is equal to 0.12 (apparently due to low roughness of coatings). In the next stage (after 2.5 m of friction Figure 15a) coating starts to destruct (appearance of potholes, cracks) – it is an abrasive wear (Figure 15b). The friction coefficientincreases to 0.45 (it indicates that the coating is not of high hardness).
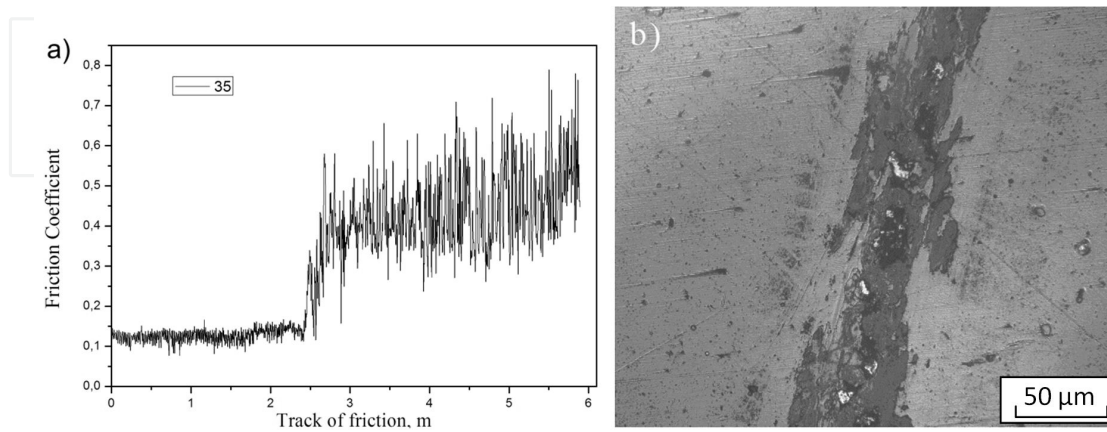
Figure 15. a) dependence of friction coefficient on friction track, b) image of the sample's №35 wear track.

Figure 16(a) represents results of tests on scratch-tester REVETEST of sample 23 with next characteristics: LC1=2,46N and LC2=10,25N.

As the criterion of adhesion strength the critical loading LC, which resulted in destruction of coating, was accepted. However, to treat the results of coatings testing many researchers use the lower (LC1) and overhead (LC2) critical loadings, which characterize ah adhesion strength. Lower critical loading (LC1) is the loading, under which initial destruction of coating occurs Figure 16 (b). And the overhead critical loading (LC2) is the loading under which the coating fully exfoliates from substrate. For samples 23 the lower critical loading for our coverage is LC1=2,46 N and overhead critical loading of LC2=10,25 N, which characterizes a good adhesion/cohesion strength. [12-14]
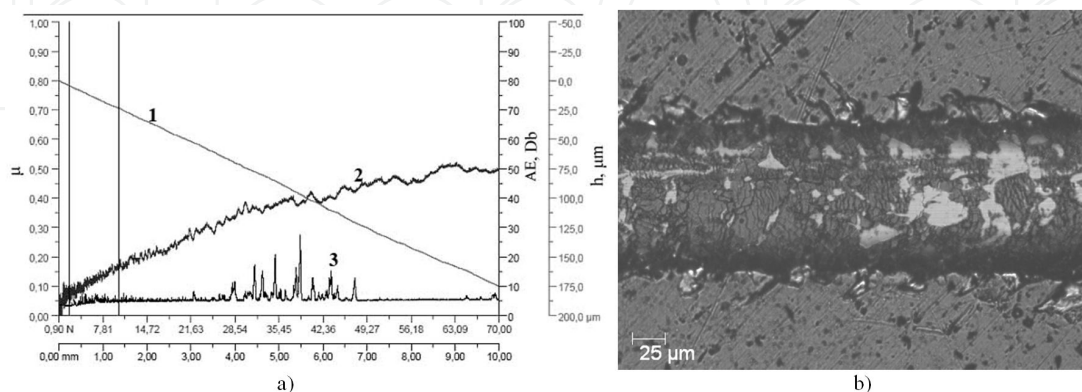
Figure 16. The results of adhesion tests of Ti-Hf-Si-N/substrate/steel coatings system on sample 23: a) 1-penetration depth, 2-Friction Coefficient (µ) and 3-dependence A_E; b) coating structure in destructions zone in load ranges 0,9 – 90 N.

6. Properties of nanostructured coatings Ti-Hf-N (Fe)

As we know, uniqueness of nanostructure nanocomposite coatings is a high volume fraction of phase boundaries and their strength, in the absence of dislocations inside the crystallites and the possibility of changing the ratio of shares of the crystalline and amorphous phases, and also the mutual solubility of metallic and nonmetallic components.

The formation of local sections of Al and C ion implantation of Al in α-Fe due to the process of segregation and the formation of helicoids were found by using microbeam ion, positron annihilation and electron microscopy in works, as increase the diffusion processes N + ions in ion-plasma modification were showed in works.

The films consisted of Ti-Hf(Fe) were deposited on steel samples with diameter of 20 and 30 mm and thick in 3 mm with vacuum-arc source in the HF (High - Frequency) discharge, where fused cathode from Ti-Hf(Fe) was used (by electron gun in an Ar atmosphere). The camera unit was filled with atomic N at various pressures and potentials on substrate for nitrides obtainment. Deposition parameters are presented in Table 6.

N°	P, nitrogen pressure in the camera, Pa	Average crystals size, nm	Hardness, GPa	Substrates potential, V
7(direct)	0,3	6.5	41.82	-200
11(separ)	0,5	4.8	47,17	-200

Table 6. The results of deposition coating Ti-Hf-N (Fe).

A scanning nuclear microprobe based on the electrostatic accelerator IAP NASU was used for analyze the properties of the coatings of Ti-Hf-N (Fe). The analysis was performed using the ions Rutherford backscattering (RBS), the characteristic X-ray emission induced by protons (PIXE and μ - PIXE) at the initial energy Ep = 1,5 MeV, the beam size (2 ÷ 4) μm, the current ≈ 10^{-5}A. PIXE analysis of the overall spectrum was performed using GUPIXWIN program, which allowed us to obtain quantitative information about the content of elements and stoichiometry. For comparison, the scanning electron-ion microscope Quanta 200 with EDS was used for elemental composition and morphology.

We used a vacuum-arc source "Bulat - 3T" with RF generator. Potential bias was applied to a substrate by HF - generator, which produced pulses of damped oscillations with a frequency ≤ 1 MHz pulse with a 60 μs, with a repetition rate of 10 kHz. The magnitude of the negative self-bias potential on the substrate by HF diode effect ranged from 2 to 3 kV. Additionally a detector with a resolution of 16 keV was used with RBS He^+ ions with energies up to 1,3 MeV, θ = 170º. Value of helium ions μ≈5.

Mechanical properties were researched: hardness and nanohardness, elastic modulus with two devices Nanoindentor G 200 (MES System, USA) using a pyramidal Berkovich, Vickers and also indenter like "Rockwell C" with a radius of curvature of about 200 μm was used.
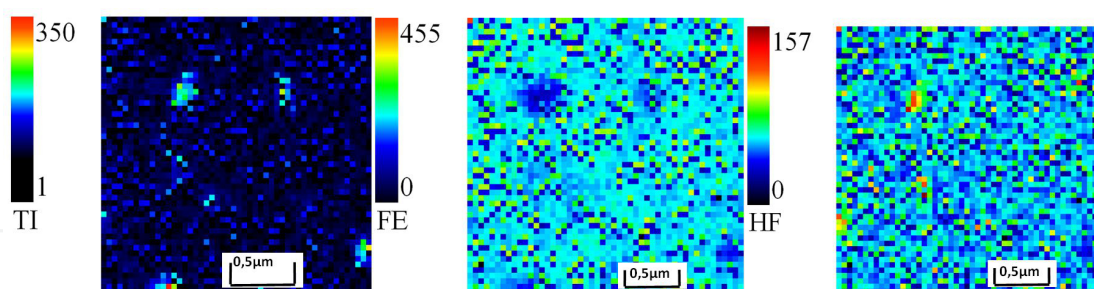
Figure 17. Maps of the distribution of elements (Ti; Hf; Fe) were obtained on samples deposited with a coating of Ti-Hf-N (Fe). In particular, see the local area the size of (2 ÷ 4) to (6 ÷ 10) μ m inclusions consisting of Hf, Ti, which sharp decreases the concentration of Fe.

As seen from these figures cover is different heterogeneity distribution of the elements Ti, Hf, Fe on the surface and the depth of coverage. Quantitative analysis and stoichiometry obtained by PIXE is shown in Figure 17. As seen from the results (integral concentration over the depth about 2 μm) a thin film of AlCformes on the surface, which is probably the result of exposure to the proton beam, and the main elements of the concentration of Fe ≈ 77%, Ti ≈ 11%, Hf≈ 11 05, Mn≈ 0,9% and Cr = 0.01%, the latter elements are apparently part of the substrate (Figure 18). [12,14,15]
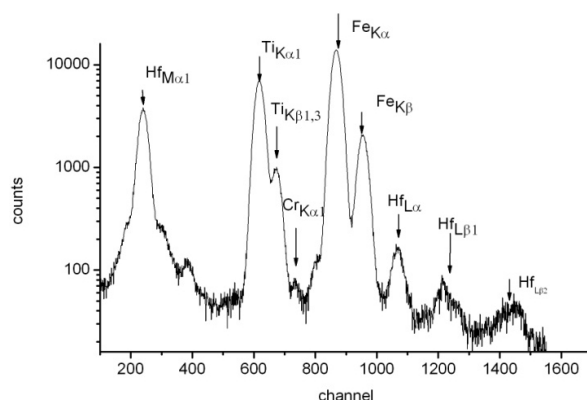
Figure 18. The mass transfers and segregations effect on formation of the super hard ≥ 48GP ananostructured coatingsTi-Hf-N (Fe).

Figure 19 (a) shows an image of the surface area coverage with the imprint of the indenter, which is equal to the value of 48,78 ± 1,2 GPa, these hardness values are very high about 50 GPa and correspond, according to modern classification as superhard coatings. The results of XRD analysis on samples, obtained with this type of coverage, show that the coating formed from at least two phases (Ti, Hf)N, (Ti, Hf)N or FeN, and the size of the nanograins certain width of diffraction peaks of Debye-Scherrer up (4,8-10,6) nm. Using foil, obtained from the coating with a TEM analysis it was found that the coating is formed by a mixture of phases, nanocrystalline (Ti, Hf)N with a grains size 3,5 ÷ 7,2 nm and quasi-amorphous, apparently, FeN. Three-dimensional islands on films surface with columnar structure come to facets surface of individual grains (Figure 19a).
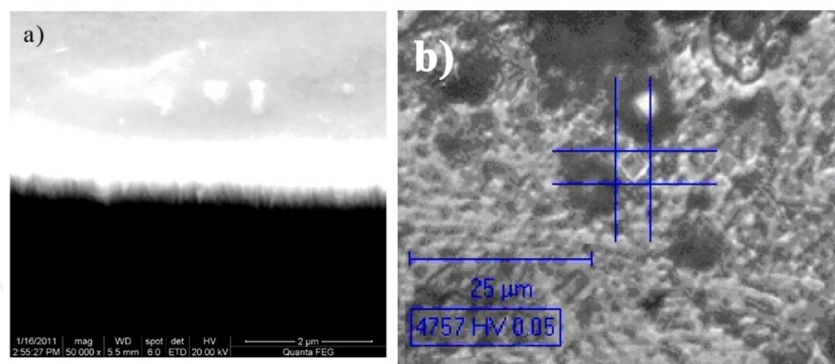
Figure 19. a,b) The mass transfers and segregations effect on formation of the superhard ≥ 48GP ananostructured coatings Ti-Hf-N (Fe).

It is seen that the surface roughness depends on the chemical composition and deposition parameters as well. Surfaces undulation associated with the mechanism of growth and the formation of separate islands on the surface (Volmer-Weber mechanism). At the same time compression microstresses were found (by measuring the XRD spectra in the geometry of up to 2 $\theta\theta$, and using the method of $\sin2\ \varphi$) in the coating which are formed in nanograin and the corresponding value ≈ 2,6%.

Compressive stresses arise in the growth plane of the film obtained by the width of the diffractions lines peaks according to the method $\sin^2\varphi$ was about ≈ 2,78%. With the plasmas beam separation derived textured coatings with varying degrees, so for example, if the application to a substrate of high potential (-100V) - this texture with pin [110]. In the case of the formation of nanocomposites with TiN-nc and the α-Si$_3$N$_4$ (in the form of quasi-amorphous phase) of a thickness of less than 1N (about a monolayer) coatings are formed with very high hardness (superhard) 80 GPa. A necessary and sufficient condition is the end of the process of spinodal segregation at grain boundaries, but this requires a high substrate temperature during deposition (600-650°C) or a sufficiently high rate of diffusion as In our case the substrate temperature during deposition did not exceed 300°C, then apparently, the process of spinodal segregation is not completed [15].

7. Hard nanocomposite coatings with enhanced toughness

A thin coating was formed using vacuum-arc source and followed the coating surface relief formed by plasma-detonation. Its average roughness varies from 14 to 22 μm (after melting and coating deposition using vacuum-arc source). An image of X-ray energy dispersion spectrum is presented below. It indicates the following element concentrations in the thin coating: N ~ 7.0 to 7.52vol.%; Si ~ 0.7vol.%; Ti ~ 76.70 to 81vol.%. For the thick coating we found Fe ~ 0.7vol.%, and traces of Ni and Cr.

Figure 20 presents RBS data for the thick (Cr$_3$C$_2$)$_{75}$-(NiCr)$_{25}$ coating without Ti-Si-N thin one. Results for combined coating are presented below, Figure 20.

Element distribution, which was calculated according to a standard program, indicated N = 30at.%; Si ≈ 5 to 6at.%; Ti ≈ 63 to 64at.%. Spectrum of thick coating did not allow us to evaluate element concentration due to high surface roughness of the coating formed by plasma-detonation method.
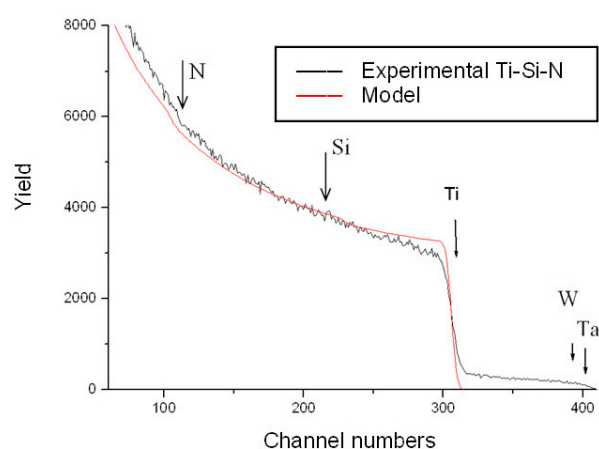

Figure 20. Energy spectra of Rutherford ion backscattering (RBS) for top thin coating Ti-Si-N/WC-Co-Cr.

Special samples were prepared for hardness measurements. Their surfaces were grinded and then polished. After grinding, thickness of $(Cr_3C_2)_{75}$-$(NiCr)_{25}$ thick coating decreased to 80 - 90μm. Thin Ti-Si-N film of about 3μm was condensed to the grinded surface. As a result, we found that hardness of different regions essentially varied within 29 ± 4 GPa to 32 ± 6GPa. Probably, it is related to non-uniformity of plasma-detonation coating surface, which hardness varied up 11.5 to 17.3 GPa. These hardness values remained after condensation of Ti-Si-N thin coating Elastic modulus also features non-ordinary behavior. [16]

Hardness of the thin coating, which was deposited to a polished steel St.45(0.45 % C) surface had maximum value of 48GPa, and its average value H_{av} was 45GPa. Variation of hardness values was lower than that found in a combined coating.

Figure 21 shows dependences of loading-unloading for various indentation depths. These dependences and calculations, which were performed according to Oliver-Pharr technique, indicated that hardness of Ti-Si-N coatings deposited to thick $(Cr_3C_2)_{75}$-$(NiCr)_{25}$ was 37.0 ± 4.0GPa under E = 483GPa.

These diffraction patterns and calculations of coating structure parameters. In the coating, basic phases are Cr_3Ni_2 for the bottom thick coating and (Ti, Si)N and TiN for the thin top coating. Diffraction patterns were taken under cobalt emission. Additionally, we found phases of pure Cr and low concentration of titanium oxide (Ti_9O_{17}) at interphase boundary between thin-thick coatings. Peaks of Ti-Si-N and TiN coincided because of low Si content. (Ti, Si)N is solid solution based on TiN (Si penetration). The phases are well distinguished at 72 to 73° angles.
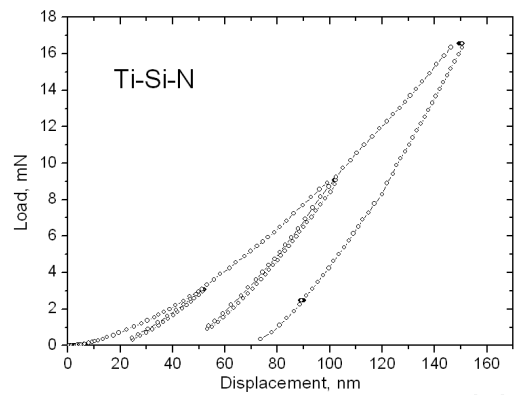
Figure 21. Loading-unloading curves for Ti-Si-N/WC-Co-Cr coating under various Berkovich indentation depths.

Figure 22 a, b shows regions of thick bottom $(Cr_3C)_{75}$-$(NiCr)_{25}$ coating and intensity distribution of X-ray emission (Figure22 c, d) for basic elements. In this coating, content of basic elements is the following: nickel and chromium - 36wt.% and 64wt.%, respectively. Also, we found carbon, oxygen, and silicon. Transversal cross-sections did not allow us to distinguish thin upper coating due to its low thickness. We found regions for pure nickel and chromium. Nickel matrix (a white region) indicated high amount of chromium inclusions with various grain sizes: small grains of < 1µm, average – of 4 to 5µm, and big – of 15 to 20µm. The white region is reach in Ni (to 90at.%). A grey region is reach in Cr (to 92at.%). In these experiments, we failed to determine composition and thickness of Ti-Si-N because of its small thickness. However, 7° angular cross-sections allowed us to find Ti-Si-N element composition and composition of the bottom thick layer $(Cr_3C_2-)_{75}(NiCr)_{25}$ by 10 to 12 points. [16-18]
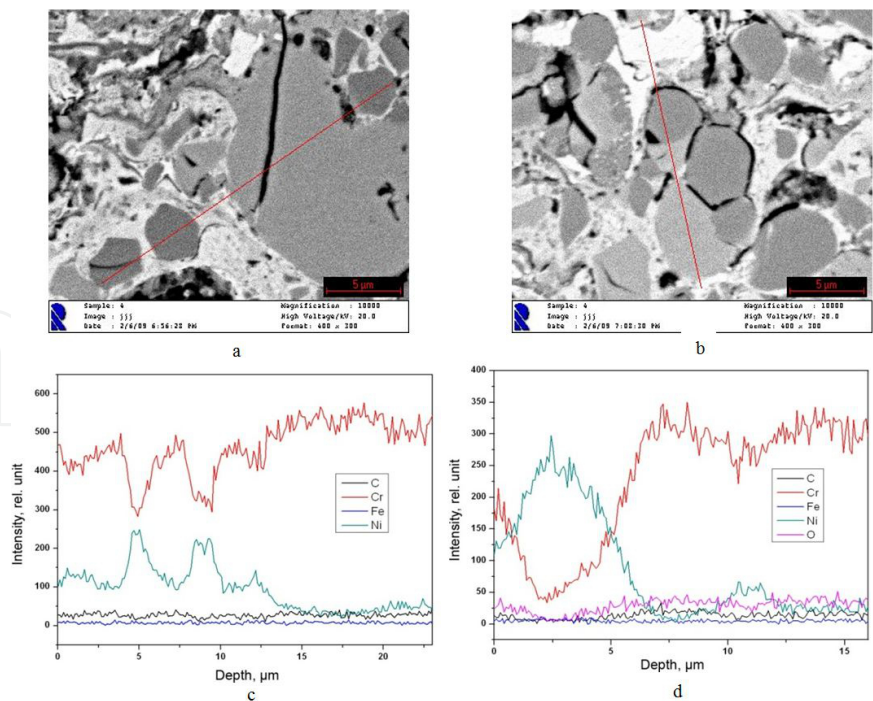
Figure 22. a, b - Regions of transversal cross-section for combined coatings (lines of element analysis are indicated) from SEM and EDS analyses. c, d - Element distribution over depth of combined coating Ti-Si-N/$(Cr_3C_2)_{75}$-$(NiCr)_{25}$ for the regions indicated in a, b.

8. Industrial Applications

It is well known that investigation of nanostructured objects is the most quickly progressing field of modern material science, since a superfine disperse structure is a reason for significant and, in some cases, crucial change of material properties.

Investigations of materials with superfine grain structures demonstrated that when a crystal grain size decreased below some "threshold value", material properties change crucially. This size effect manifested itself even in the case, when an average crystal grain size did not exceed 100 nm. However, it became more pronounced for materials with grain size ranged within 10 nm, and the intercrystalline (intergrain) distances were about few nanometers, contained mainly amorphous phases (nitrides, oxides, carbides, etc.). Stresses, occurring inside these interfaces, are contributed to the increase of the nanocomposite coating deformation resistance, and an absence of inside crystallite dislocations provides with improvement of the coating elasticity. [17]

In this work, we present the first results of investigation of a structure and properties of a new type nano-and microstructure Ti-N-Cr/Ni-Cr-B-Si-Fe-based protective coatings fabricated by the plasma-detonation technology and subsequent vacuum-arc deposition. The aim of this work was fabrication and investigation of the structure, physical and mechanical properties of micro-nanostructured protective coatings with thickness from 80 to 90 μm based onTi-N-Cr/Ni-Cr-B-Si-Fe. Bilayered coatings allowed us not only to protect tools from abrasive wear, but also to recover their geometrical dimensions within 60 to 250μmand more.

We selected a thick coating PG-19N-01 (Russian standard) (Cr-B-Si-Fe(W), based on Ni) since alloys based on Ni-Cr (Mo) have high corrosion resistance even in the solution of acids HCl, H_2SO_4, and HNO_3+HF, under high temperatures, and Ni is able to dissolve a great amount of doping elements (Cr, Mo, Fe, Cu). It was also known that Cr in Ni alloys and Mo in nickel-molybdenum alloys stopped dissolution of a nickel base, though Cr favored and Mo made difficult a passive character of dissolution. Moreover, hardness of (Ni-Cr-B-Si-Fe(W)) powder coating was 3 to 4 times higher than that of a substrate (1.78 ±0.12) GPa. We would like to note that Ni-Cr system is a base for many refractory nickel alloys. Therefore, chromium doping of nickel leads to essential increase of high temperature oxidation resistance. [16]

Ti-N-Cr thin coating (a solid solution) was selected taking into account the considerations that its functional properties (hardness H, elasticity modulus E, plasticity index H/E, material resistance to plastic deformation H^3/E^2, and wear resistance) were notably higher than those of Ni-Cr-B-Si-Fe(W) thick coating of (110 to 120) μmthickness.

The powder was placed inside the reaction chamber and the surface coating layer of (40 to 55)μm was melted by a plasma jet, which was doped by liquid drops coming from an eroding (doping) electrode (W). Melting, which was conducted to reduce a surface roughness from (28÷33) μm to (14÷18) μm and to obtain a more uniform element distribution in the near-surface layer was employed to achieve the necessary mechanical properties. Thus, such a combination of two layers: a thick Ni-Cr-B-Si-Fe layer of 90 μm, which was deposited using plasma-detonation technology, and a subsequently deposited Ti-Cr-N thin upper layer

(with a size of the layer like units of a micron), which featured higher physical-mechanical characteristics, was selected to provide improved protective properties and restoration of worn surface regions. [18]

Figure 23a presents the SEM image of a nano-microstructured protective Ti-N-Cr coating surface region.

In the coating surface, one can see some regions with droplet fraction (they are marked with points, at which we performed microanalysis). The point 1, which was taken in the coating surface in X-ray energy dispersion (EDS) spectrum, shows N, Ti, Cr elements, and traces of Ni. Figure 23b and Table 7 show results of integral and local analyses. These results demonstrate almost the same results for N (from 0.56 to 0.98 wt.%), Ti (from 39 to 41%), and Cr (56.8 to 59.4%).We also detected Ni (0.82 to 0.98 %) in thick coating.

|	Ni	Cr	Ti	N	□
p19_int1	0.578	40.509	58.095	0.819	100.000
p19_int2	0.487	41.867	56.797	0.850	100.000
p19_2	0.564	39.073	59.390	0.973	100.000
p19_1	0.507	40.711	57.805	0.978	100.000

Table 7. Distribution of elements (EDS) on the surface of protective coating Ti-N-Cr concentration (wt.%)
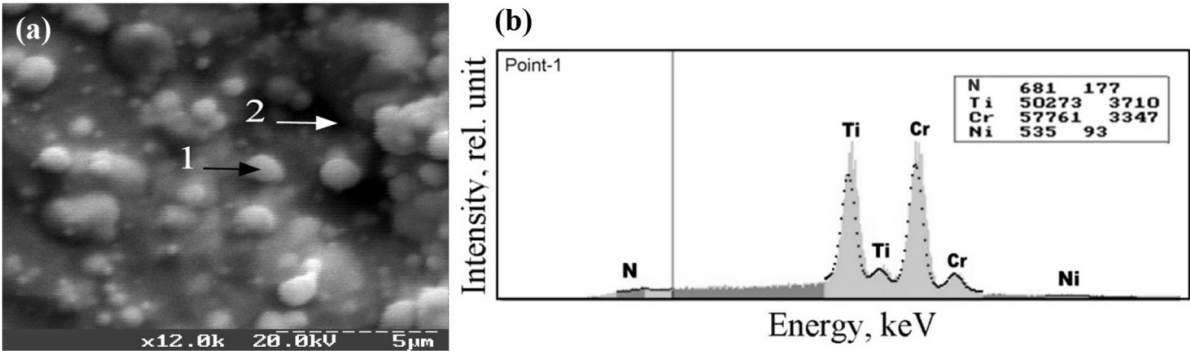
Figure 23. a) Image of the Ti-N-Cr/Ni-Cr-B-Si-Fe(W) coating surface obtained using the scanning electron microscope SEM. The photo shows the points, in which the microanalysis was taken. (b) Energy dispersion X-ray spectrum for the first of the mentioned points, see Figure23a.

Figures 24a and 24b show RBS spectra for protons (Figure 24a) and helium ions $^4He^+$ (Figure 24b). From these spectra one can see that all elements (N, C, Ti, Cr) composing Ti-N-Cr/Ni-Cr-B-Si-Fe coating were found. The fact that a "step" was present in the spectrum almost over the whole depth of analysis of this coating is worth one's attention. It indicates a uniform nitrogen distribution and formation of $(Ti\ Cr)_2N$ compounds. The compound stoichiometry was close to $Ti_{40}Cr_{40}N_{20}$ or $(Ti, Cr)_2N$.

Table 8 presented the coating composition, which was obtained using RBS and a stand-ard program. One can also mention low W concentration (0.07 at.%) in the thin coating. But near the interface between the thick and the thin coating, this concentration increased to 0.1 at.%. We assumed that W diffuse from thick coating (from the eroding electrode). The stainless steel substrate composition demonstrated Ni_3Cr_2. Comparison of RBS, EDXS, and XRD data allowed us to state that in the thin nanostructured coating (Ti-Cr-N), oxy-gen was absent (less than 0.1%), and carbon was present, but its concentration was lower than XRD detection ability.
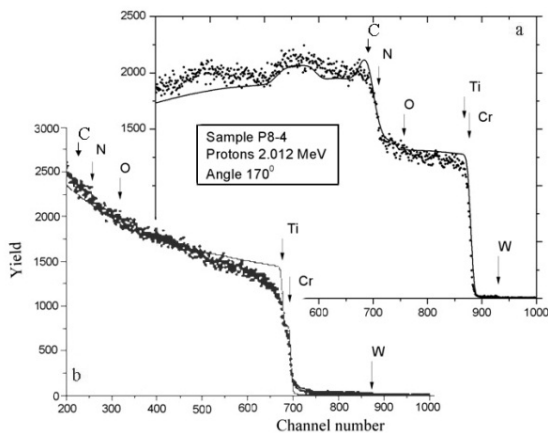

Figure 24. a, b. An energy RBS spectrum for proton scattering with the initial energy 2.012*MeV* – (a) and 2.035*MeV* – (b) taken for the sample Ti-N-Cr/Ni-Cr-B-Si-Fe(W). The arrows indicate the boundaries of kinematical factors for differ-ent elements.

Depth	Concentration (at. %)				
Nm	W	Ni	Cr	Ti	N
625	0.07	0	38.70	38.70	22,52
1251	0.07	0	38.70	38.70	22,52
2317	0.09	0	38.70	38.70	22,52
3263	0.09	0	38.70	38.70	22,52
14380	0	61.30	38.70	0	0

Table 8. Distribution of elements on the depth of protective coating Ti-N-Cr.

The general views (their cross-sections) of these coatings are presented on Figures 25 a, b.

Figure 25a shows the sample without coating. The right part of this Figure demonstrates da-ta of micro-analysis ("A-A'" cross-section). An etched coatings layer was almost free of pores. The interface between the coating and the substrate was wavy; this indicates penetra-tion of powder particles to the substrate.
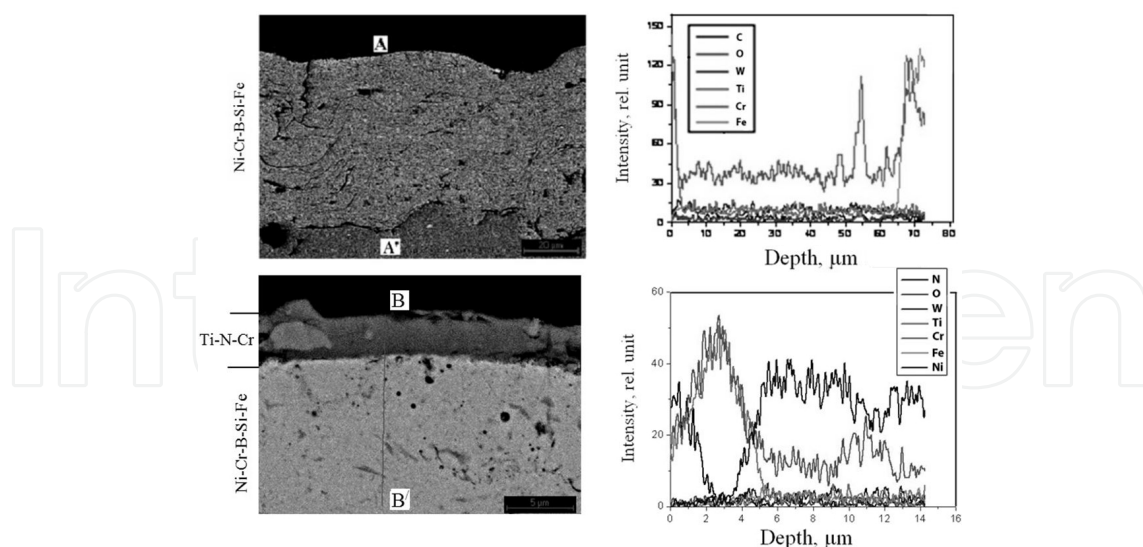
Figure 25. a) Scanning electron microscopy images for the cross-section (A-A') and distribution of the characteristic X-ray element emission over this cross-section (A-A') in a combined nanocomposite coating (a thick coating was melted by a plasma jet). (b) Scanning electron microscopy images for the cross-section and distribution of the characteristic X-ray element emission along the cross-section (B-B') in the coating on the base of (Ti, Cr)N solid solution. The thin coating was deposited on the thick one of Ni-Cr-B-Si-Fe(W) and melted by a plasma jet.

Figure 25b shows a cross-section for Ti-N-Cr/Ni-Cr-B-Si-Fe coating. Its element distribution over cross-section depth is demonstrated in the right part of Figure 25b ("B-B'"). The thin coating was composed of Ti and Cr (N was not found, possibly due to low detector resolution). Results of XRD analysis for Ti-N-Cr/Ni-Cr-B-Si-Fe coating are presented in Table 9. Calculation of diffraction patterns (Table 9) demonstrated (Ti, Cr)N (200) and (Ti, Cr)N (220). Additionally, γ – FeNi$_3$ and FeNi$_3$ phases were found in these samples. Also we have determined that diffraction peaks were shifted, under-peak areas differed, and derived ratios of intensities. Measurements and analysis of diffraction lines, which were taken using grazing incidence diffraction, demonstrated smoothed peaks corresponding to amorphization or formation of nanocrystalline phases. [16-18]

| 2θ degree	Area	Intensity	Semi width	Value Angstrom	Relative Intensity	Phase	HKL
43,100	67,883	53	2,4450	2,0987	58,89	(Ti,Cr)N	200
43,640	24,025	90	0,5200	2,0740	100,00	□-(Fe,Ni)	111
50,840	6,066	27	0,4450	1,7959	30,00	□-(Fe,Ni)	200
63,020	1,693	19	0,1800	1,4750	21,11	(Ti,Cr)N	220
74,400	5,358	19	0,5500	1,2750	21,11	□-(Fe,Ni)	220
90,620	5,130	20	0,5000	1,0844	22,22	□-(Fe,Ni)	311
96,060	1,892	19	0,2000	1,0368	21,11	□-(Fe,Ni)	222

Table 9. Calculation results of diffraction patterns of Ti-N-Cr coating from the side of thin coating.

In addition to basic phases, an X-ray diffraction, which was performed at 0.5° angle, demonstrated also simple hexagonal compounds Cr_2Ti, Fe_3Ni (Fe, Ni) and various compounds of a titanium with nickel Ti_2Ni, Ni_3Ti, Ni_4Ti_3, etc. (Figure 26a). These additional phases were formed at some initial stages of the coating deposition, as a result of titanium, nickel, chromium and iron diffusion. A resulting solid solution was a small-grain dispersion mixture (grain size were calculated according to Debay-Sherer formula and reached about 2.8 to 4 nm) (Figure 26b).
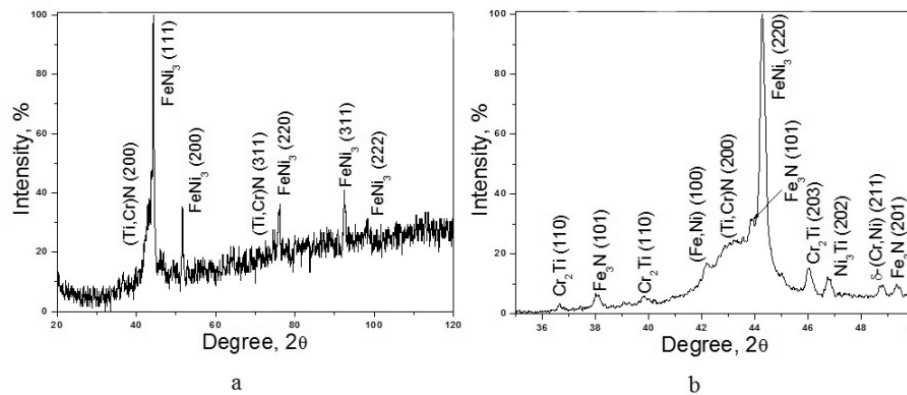

Figure 26. Fragments of the diffraction patterns taken in the incidence grazing diffraction for the whole region (a) and for the selected intensity peak (b).

TEM analysis (Figure 27a, b) demonstrated that an order of nanograin size magnitude corresponded to XRD data, namely ranged within 5 to 12 nm. (Ti, Cr)N lattice of a solid solution corresponded to NaCl, see the diffraction data in Figure 27a. The light field analysis demonstrated a uniform distribution of nanograins of various sizes (Figure 27b.), which correlated well with results reported in paper. In this report, Ti-Cr-N was deposited from two cathodes using VAD under the same coating nanohardness, which amounted from 32.8 to 42.1 GPa.
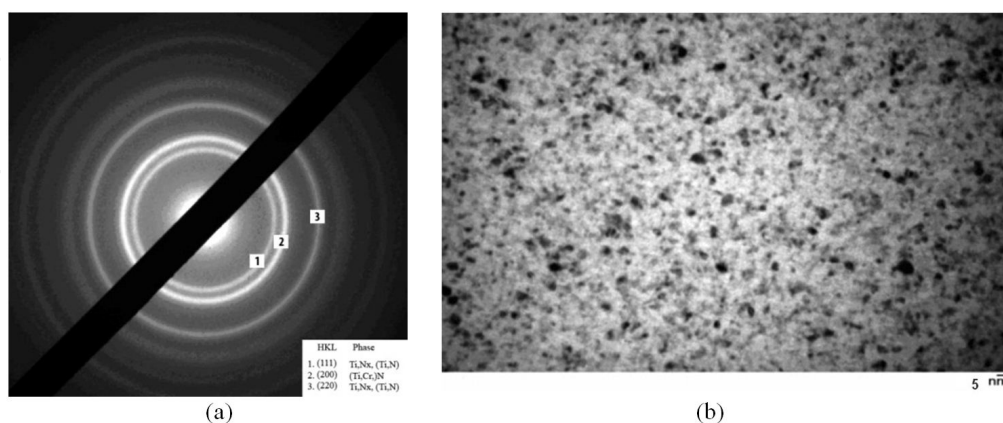
Figure 27. a) Electron diffraction patterns for nanocomposite coatings, cubic phase of solid solution (Ti,Cr)N, with NaCl type lattice. (b) Light-field image for nanocomposite films fabricated from thin coating based on (Ti,Cr)N solid solution phase.

High magnification allowed us to see a mixture of differently oriented nano-grains (Figure 28a). Interfaces of the nano-grains were not separated, and we failed to find an expressed symmetry in positions of the nano-grains and a definite orientation of atomic planes. However, the electron diffraction patterns of the studied regions demonstrated clearly visible point reflexes, which coincided with the ring electron diffraction pattern of the coating matrix (Figure 28b). Sizes of individual nano-grains reached from 2 to 3 nm, but point reflexes indicated the formation of micro-regions with identically-oriented crystalline lattices. Nevertheless, interfaces of such formations were not pronounced.

(a)   (b)
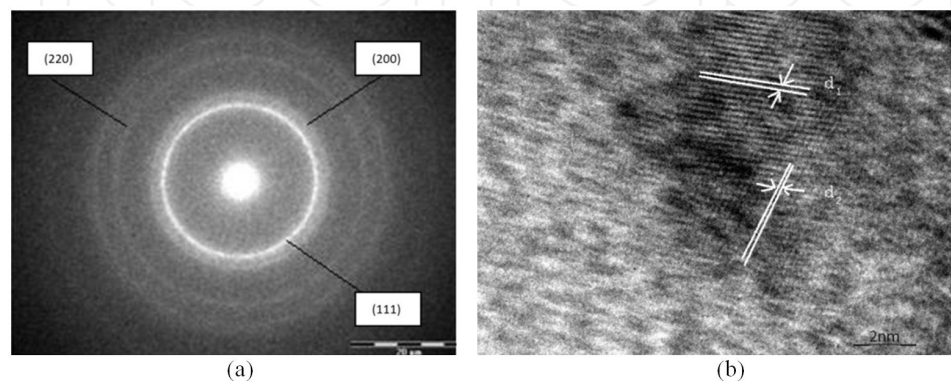
Figure 28. a) Electron diffraction from the matrix of the Ni-Cr-B-Si-Fe coating, indicating the indices of the crystallographic planes. (b) High resolution image of Ni-Cr-B-Si-Fe interface, with the presence of nanoscale domains of crystallographic orientation which coincided with the ring electron diffraction pattern.

The obtained results allowed us to conclude that an inter-metalloid $Cr-Ni_3$-phase having a fcc-lattice was formed in the coating surface. It was found that chromium compounds were formed only in a thin surface coating layer. It is evident that a main reason for the non-uniform phase formation was a non-uniform temperature profile, which was formed over the sample depth under an action of a plasma jet.

It was also found that a thin layer, which was formed in the sample surface after treatment, contained oxides, carbides and various phases of the coating elements, which badly dissolved under high temperatures. A basic coating layer featured an essentially uniform phase composition and contained a γ-phase, a solid solution on nickel base, and α-phase based on iron. The latter was found only on the coating side, which was adjacent to the substrate.

Taking into account the fact that at 700°C to 800°C temperatures, a carbide hardening phase of alloys based on Ni-Cr-B-Si-Fe coagulated faster than the intermetalloid one, we assumed that one should prefer to employ alloys with an intermetalloid type of solidification.

A partial spectrum I corresponded to stainless steel. Some asymmetry, which was observed in a quadruple duplet (various amplitudes and widths, but similar areas of resonance lines), was due to the non-uniformity in surrounding Fe atoms.

The partial spectrum II corresponded to α – Fe particles. In comparison with a standard α – Fe spectrum, these values of a Mössbauer line shift δ and a quadruple ϵ, which differed

from zero, and a little lower value of superfine field indicated nanosized impurities ≤ 100 nm (in locally non-uniform systems). [9,11,16]

The coating surface and cross-section morphology was additionally studied using an electron scanning microscopy SEM and X-ray spectral micro-analysis (using LEO-1455 R microscope). A thin coating Ti-Cr-N based on solid solution fully repeated substrate relief.

Samples with Ti-Cr-N coatings had 6.8 and 8.4 mkg/year corrosion rate, depending on thin layer composition (stoichiometry) (Figure 29).
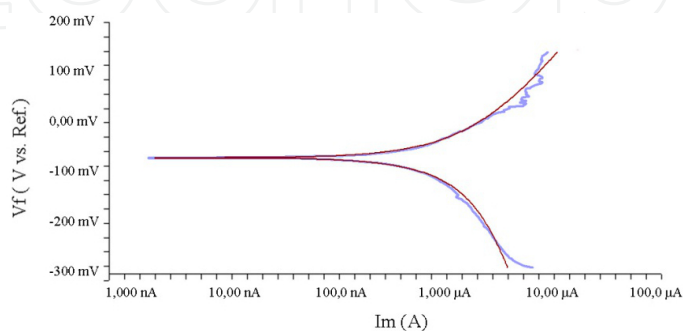
Figure 29. Experimental dependences of corrosion and Tafel curves for the sample Ti-Cr-N/Ni-Cr-B-Si-Fe(W).

The hardness H and elasticity modulus E were determined using the nanoindentation device Nanoindenter II, according to Oliver and Pharr methods and with the help of a Berkovicz indenter, see Figure 30. For a surface layer, a value of elastic recovery W_e was calculated using loading-unloading curves, according to the formula

$$W_e = \frac{h_{max} - h_r}{h_{max}} \tag{1}$$

where h_{max} was a maximum penetration depth, and h_r was a residual depth after a load relieve.

It was obtained that the elasticity modulus of Ti-Cr-N coating had a value $E_{mean} \sim 440$ GPa, its hardness was $H_{mean} \sim 35.5G$ Pa, and the maximum value was 41.2 GPa (see the Table 10).

Table 10 and Figure 30a demonstrates highest hardness values obtained from nanoindentation measurements: (32,8 – 42,1) GPa for Ti-Cr-N, 6,8 GPa for Ni-Cr-B-Si-Fe, and 8,1 GPa for Ni-Cr-B-Si-Fe coatings after a plasma jet melting. We noticed a lower difference in hardness values in comparison with cases without melting. The substrate hardness was 1.78 ± 0.14 GPa. The elasticity modulus was also higher for Ti-Cr-N coatings and amounted 360 ÷ 520 GPa (Figure 30b). It was 229 ± 11 GPa for Ni-Cr-B-Si-Fe coating after the plasma jet melting.

To evaluate a material resistance to an elastic strain failure, the authors used a ratio of hardness to the elasticity modulus H/E, which was named a plasticity index. To evaluate the material resistance to a plastic deformation, they used, for example, H^3/E^2 ratio. So, to increase a resistance to an elastic strain failure and plastic deformation, a material should have a high

hardness and a low elasticity modulus. As it is known from, typical ratios for ceramics and metallic ceramics did not exceed 0.2 GPa. For NiTi, due to a form memory effect, it was lower by an order of magnitude. New nanostructured materials, which were obtained in our experiments, demonstrated H^3/E^2 ratios ranging within 0.29 ± 0.03. Many materials featuring high H^3/E^2 ratios indicated a high wear resistance. And the elasticity modulus of deposited materials was close to the Young modulus of materials with high H^3/E^2 ratio, which indicated high wear resistance. Used materials resistance to plastic deformation, we used same coating nanohardness, which amounted 32.8 to 41.2 GPa one of the substrate material. These indicated high servicing characteristics under abrasive, erosion, and impact wear conditions.
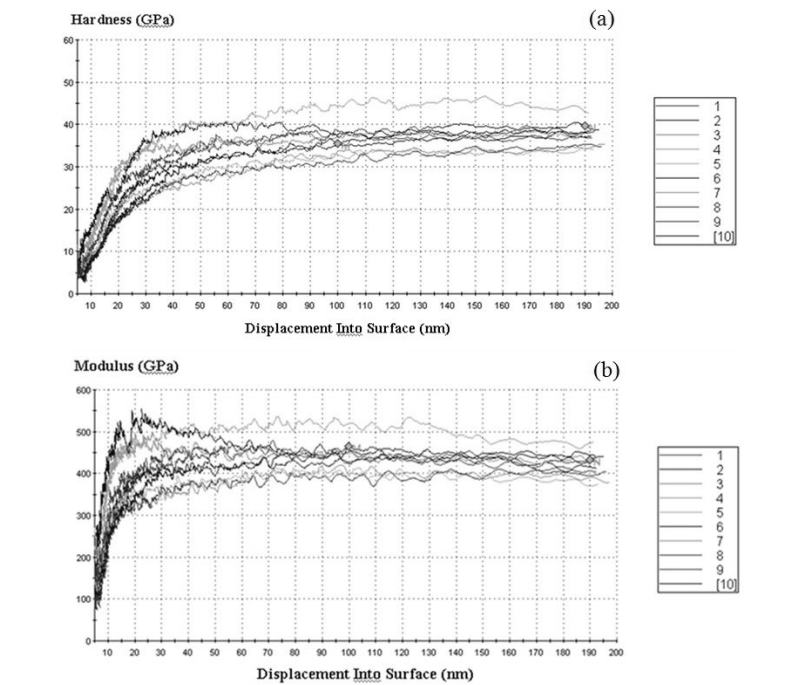

Figure 30. Curves for hardness H (a) and elasticity modulus E (b) obtained for the sample Ti-N-Cr/Ni-Cr-B-Si-Fe. The calculation results for H and E are presented in the Table 10.

Coating material	E, GPa	H, GPa
Ti-N-Cr	360 - 520	32.8 - 41.2
Ni-Cr-B-Si-Fe (W)	193±6	6.8±1.1
Ni-Cr-B-Si-Fe (W) (Melting of Plasma jets)	217±7	8.1±0.2
Substrate	–	–
(NiCr)	229±11	1.78±0.14

Table 10. Results of mechanical characteristics tests, being obtained by nanoindenter.

Therefore, we performed measurements of the wear resistance under the cylinder friction over nanocomposite combined coating surfaces without lubrication. Results of these tests are presented in Figure 31. As it is seen from the Figure 31, the maximum wear resistance of a nanostructured Ti-Cr-N coating was a factor from 27 to 30 lower than that of a steel substrate. A low wear was also observed in thick Ni-Cr-B-Si-Fe coating melted by a plasma jet. Samples coated by Ni-Cr-B-Si-Fe, which were stored in air, in a wet environment for 5 to 7 years, after repeated melting by a plasma jet demonstrated unchanged hardness, elasticity modulus, corrosion resistance, which stayed almost the same within the limits of a measurement error that undoubtedly seems to be promising for protection of steels and alloys.
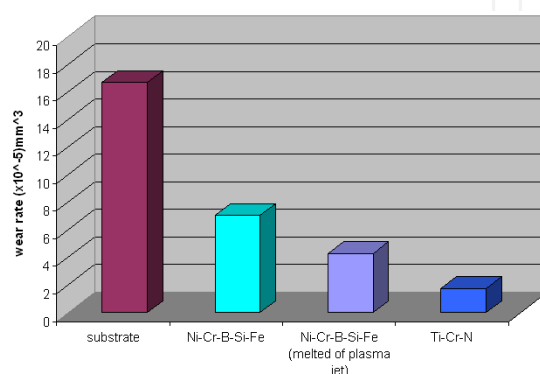
Figure 31. Histograms of dependences of wear rates for samples, which were fabricated according to scheme cylinder-plane.
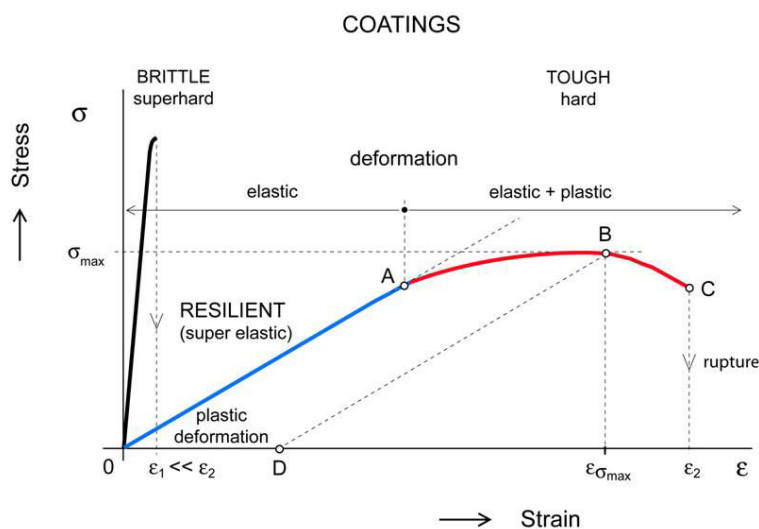
9. Hard nanocomposite coatings with enhanced toughness

Hard nanocomposite coatings with enhanced toughness are coatings which are simultaneously hard and tough. Such coatings should be very elastic, exhibit a low plastic deformation, resilient properties when the plastic deformation is zero, and an enhanced resistance to cracking.

The way how to produce hard, tough and resilient coatings is indicated by the Hooke's law $\sigma = E.\varepsilon$; here, σ is the stress (load), ε is the strain (deformation). If we need to form the materialwhich exhibits a higher elastic deformation (higher value of ε) at a given value σ its Young'smodulus E must be reduced. It means that materials with the lowest value of the Young'smodulus E at a given hardness H (σ=const) need to be developed. It is a simple solution but avery difficult task.

The stress σ vs strain ε dependences for brittle, tough and resilient hard coatings areschematically displayed in Figure 32. Superhard materials are very brittle, exhibit almost n plastic deformation and very low strain $\varepsilon=\varepsilon_1$. Hard and tough materials exhibit both elastic and plastic deformation. The material withstanding a higher strain $\varepsilon_1 \ll \varepsilon \le \varepsilon_{max}$ without it cracking exhibits a higher toughness. The hardness of tough materials is higher in the case when ε_{max} is achieved at higher values of σ_{max}. On the contrary, fully resilient hard coatings exhibit, compared to hard and tough materials, a lower hardness H, no plastic deformation

(line 0A) and high elastic recovery We. The hardness H of hard, tough and well resilient coatings, ranging from about 15 to 25 GPa, is, however, sufficient for many applications. The main advantage of these coatings is their enhanced resistance to cracking. These are reasons why in a very near future the hard and tough, and fully resilient hard coatings will be developed. These coatings represent a new generation of advanced hard nanocomposite coatings.

Figure 32. Schematic illustration of stress σ vs strain ε curves of superhard (brittle), hard (tough) and hard (resilient) coatings. Resilient coatings exhibit no plastic deformation (line 0A) [19].

We can conclude that a new task in the development of advanced hard nanocomposite coatings with enhanced toughness is to produce coatings with (i) a low value of the Young'smodulus E* satisfying H/E*≥ 0.1 ratio and (ii) a high value of the elastic recovery We. The coatings fulfilling these requirements can be really prepared if the element added into a base material is correctly selected as is shown in Figure 33. [20-24]

Figure 33 displays H=f(E*) dependences of five Ti-N, Ti-Al-N, Zr-N, Zr-Cu-N and Al-Cu-Nnitride coatings prepared by magnetron sputtering. Also, in this figure a straight lineH/E*=0.1, which divides the H-E* plane in two regions with H/E*>0.1 and H/E*<0.1, is displayed. From this figure it is seen that experimental points corresponding to individual nitrides are quite well distributed along mutually separated straight lines. This figure clearly shows that (1) the coating material with the same hardness H and different elemental composition can exhibit different values of the effective Young's modulus E*, (2) the value ofE* of the Me_1-Me_2-N coating depends not only on the element Me_2 added to the Me_1N binary nitride but also on the element Me_1 which forms the binary nitride, (3) not all nitrides exhibit H/E*>0.1 and (4) the coating material with the ratio H/E*>0.1 can be achieved only in the case when both elements Me_1 and Me_2 are correctly selected. The last fact represents a huge potential for new industrial applications, particularly, for the improvement of properties of the binary nitrides and the development of new advanced protective coatings, for instance, for the improvement of cutting properties and lifetime of cutting tools.
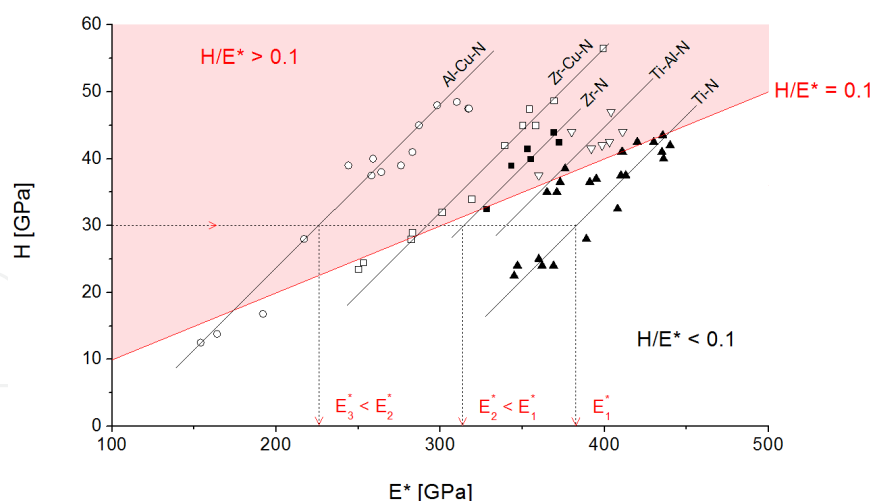
Figure 33. Control of the effective Young's modulus E* of the binary nitrides by addition of selected elements. Adapted after reference [19].

The preparation of the coatings with H/E*>0.1 is complex and difficult task because the hardness H and the effective Young's modulus E* are two mutually coupled quantities. The magnitudes of H and E* depend on deposition parameters used in the preparation of coating and are controlled not only by its elemental composition as shown above but also by its structure, phase composition and microstructure, i.e. by the energy delivered to the growing film particularly by bombarding ions and condensing atoms. At present, there are no general rules which allow predict how to prepare the coatings with H/E*>0.1. [9]

10. Trends of next development

Next research activity in the field of hard nanocomposite coatings is expected to be concentrated mainly on the solution of the following problems: (1) the development of hard coatings with enhanced toughness and increased resistance to cracking, (2) the investigation of DNG/AM composite coatings composed of small amount of nanograins dispersed in the amorphous matrix with the aim to develop new coatings with unique physical and functional properties, (3) the investigation of the electronic charge transfer between nanograins with different chemical composition and different Fermi energies in nanocomposite coatings with the aim to understand its effect on the functional properties of coating, (4) the nanocrystallization of amorphous materials at temperatures of about or less than 100°C for flexible electronics, (5) the formation of high-temperature phases at temperatures T≤500°C using superfast heating and cooling at atomic level, (6) the development of nanocomposite coatings thermally stable above 1500°C and protecting the substrate against oxidation at temperatures up to ~2000°C, (7) the formation of multilayers composed of nano-bilayers, (8) high-rate reactive deposition of hard coatings based on oxides with deposition rate a_D exceeding 10 000 nm/min, and (9) the development of new Physical Vapour Deposition (PVD) systems for the production of new advanced coatings under new physical conditions, for instance, the magnetron with molten target. [8,9, 20-25]

11. Conclusion

A current state of production and a progress achieved in investigation of properties and structures of superhardnanocomposite coatings are considered in the Chapter. The potential of various technologies employed for deposition of such coatings as Ti-Zr-Si-N, Ti-Hf-Si-N, Ti-Si-N, Ti-N, etc. is demonstrated. Investigation results obtained for micro-, nano-, and combined coatings such as Ti-Si-N / Cr_2C_3 – NiCr, Ti-N-Cr/Ni-Cr-B-Si-Fe featuring not only high nanohardness but also good corrosion resistance to NaCl, HCl, and H_2SO_4, high friction wear resistance, and very high thermal stability up to 900°C are described.

Acknowledgements

Author details

A. D. Pogrebnjak[1*] and V. M. Beresnev[2]

*Address all correspondence to: alexp@i.ua

1 Sumy State University, Sumy Institute for Surface Modification, Ukraine

2 Kharkov National University, Kharkov, Ukraine

References

[1] Gleiter, H. (1989). Nanocrystalline materials. *Progress in Materials Science*, 33, 223-315.

[2] Vepřek, S., & Reiprich, S. (1995). A concept for the design of novel superhard coatings. *ThinSolid Films*, 265, 64-71.

[3] Gleiter, H. (1996). Nanostructured Materials: State of the art and perspectives. *Nanostructured Materials*, 6, 3-14.

[4] Musil, J. (2000). Hard and superhardnanocomposite coatings. *Surface and Coatings Technology*, 125, 322-330.

[5] Gleiter, H. (2001). Tuning the electronic structure of solids by means of nanometer-sized microstructures. *Scripta Materialia*, 44, 1161-1168.

[6] Musil, J. (2006). Physical and mechanical properties of hard nanocomposite films prepared by reactive magnetron sputtering, Chapter 10 in Nanostructured Coatings, J.T.M. DeHosson and A. Cavaleiro (Eds.) New York, Springer Science+Business Media, LCC, 407-463.

[7] Pogrebjank, A. D., Shpak, A. P., Azarenkov, N. A., & Beresnev, V. M. (2009). Structure and properties of hard and superhardnanocomposite coatings. *Physics-Uspekhi*, 52(1), 29-54.

[8] Musil, J., Šatava, V., Zeman, P., & Čerstvý, R. (2009). Protective Zr-containing SiO2 coatings resistant to thermal cycling in air up to 1400°C. *Surface and Coatings Technology*, 203, 1502-1507.

[9] Musil, J., Hromádka, M., & Novák, P. (2011). Effect of nitrogen on tribological properties of amorphous carbon films alloyed with titanium. *Surface and Coatings Technology*, 205(2), S84-S88.

[10] Pogrebnyak, A. D., Bratushka, S. N., Malikov, L. V., Levintant, N., Erdybaeva, N. K., Plotnikov, S. V., & Gritsenko, B. P. (2009). Effect of high doses of N+, N+ + Ni+, and Mo++ W+ ions on the physicomechanical properties of TiNi. *Technical Physics*, 54(5), 667-673.

[11] Pogrebnyak, A. D., Shpak, A. P., Beresnev, V. M., Kirik, G. V., Kolesnikov, D. A., Komarov, F. F., Konarski, P., Makhmudov, N. A., Kaverin, M. V., & Grudnitskii, V. V. (2011). Stoichiometry, phase composition, and properties of superhard nanostructured Ti-Hf-Si-N coatings obtained by deposition from high-frequency vacuum-arc discharge. *Technical Physics Letters*, 37(7), 636-639.

[12] Beresnev, V. M., Sobol', O. V., Pogrebnjak, A. D., Turbin, P. V., & Litovchenko, S. V. (2010). Thermal stability of the phase composition, structure, and stressed state of ion-plasma condensates in the Zr-Ti-Si-N system. *Technical Physics*, 55(6), 871-873.

[13] Pogrebnyak, A. D., Sobol', O. V., Beresnev, V. M., Turbin, P. V., Dub, S. N., Kirik, G. V., & Dmitrenko, A. E. (2009). Features of the structural state and mechanical properties of ZrN and Zr(Ti)-Si-N coatings obtained by ion-plasma deposition technique. *Technical Physics Letters*, 35(10), 925-928.

[14] Pogrebnyak, A. D., Ponomarev, A. G., Kolesnikov, D. A., Beresnev, V. M., Komarov, F. F., Mel'nik, S. S., & Kaverin, M. V. (2012). Effect of mass transfer and segregation on formation of superhard nanostructured coatings Ti-Hf-N (Fe). *Technical Physics Letters (Rus)*, 38(13), 56-63.

[15] Pogrebnyak, A. D., Beresnev, V. M., Demianenko, A. A., Baydak, V. S., Komarov, F. F., Kaverin, M. V., Makhmudov, N. A., & Kolesnikov, D. A. (2012). Adhesive strength and superhardness, phase and element composition of nanostructured coatings formed on basis of Ti-Hf-Si-N. *Physics of the Solid State (Rus)*, 54(9), 1764-1771.

[16] Pogrebnjak, A. D., Danilionok, M. M., Uglov, V. V., Erdybaeva, N. K., Kirik, G. V., Dub, S. N., Rusakov, V. S., Shypylenko, A. P., Zukovski, P. V., & Tuleushev, Y. Zh. (2009). Nanocomposite protective coatings based on Ti-N-Cr/Ni-Cr-B-Si-Fe, their structure and properties. *Vacuum*, 83, S235-S239.

[17] Pogrebnjak, A. D., Ponomarev, A. G., Shpak, A. P., & Kunitski, Yu. A. (2012). Application of micro-nanoprobes to the analysis of small-size 3D materials, nanosystems and nanoobjects. *Uspekhi Phys-Nauk*, 182(3), 287-321.

[18] Pogrebnjak, A. D., Sobol, O. V., Beresnev, V. M., Turbin, P. V., Kirik, G. V., Makhmudov, N. A., Il'yashenko, M. V., Shypylenko, A. P., Kaverin, M. V., Tashmetov, M. Yu., & Pshyk, A. V. (2010). Nanostructured Materials and Nanotechnology IV- 34th International Conference on Advanced Ceramics and Composites, ICACC, Daytona Beach, FL, 24 January 2010 through 29 January 2010: Ceramic Engineering and Science Proceedings.

[19] Musil, J. (2012). Hard Nanocomposite Coatings: Thermal Stability and Toughness. *Surface and Coatings Technology*, (will be published).

[20] Mayrhofer, P. H., Mitterer, C., & Hultman, L. (2006). Microstructural design of hard coatings. *Progress in Materials Science*, 51, 1032-1114.

[21] Musil, J., Sklenka, J., & Čerstvý, R. (2012). Transparent Zr-Al-O oxide coatings with enhanced resistance to cracking. *Surface and Coatings Technology*, 206(8-9), 2105-2109.

[22] Musil, J., Šatava, V., & Baroch, P. (2010). High-rate reactive deposition of transparent SiO2 films containing low amount of Zr from molten magnetron target. *Thin Solid Films*, 519, 775-777.

[23] Musil, J. (2006). Physical and mechanical properties of hard nanocomposite films prepared by reactive magnetron sputtering, Chapter 10 in Nanostructured Coatings, J.T.M. DeHosson and A. Cavaleiro (Eds.) New York, Springer Science-Business Media, LCC, 407-463.

[24] Andrievski, R. A. (2005). Nanomaterials based on high-melting carbides, nitrides and borides. *Russian Chemical Reviews*, 74(12), 1061-1072.

[25] Patscheider, J. (2003). Nanocomposite hard coatings for wear protection. *MRS Bulletin*, 28(3), 180-183.